INTERNATIONAL JOURNAL FOR NUMERICAL METHODS IN ENGINEERING
Int. J. Numer. Meth. Engng 2012; **91**:1–26
Published online 25 April 2012 in Wiley Online Library (wileyonlinelibrary.com). DOI: 10.1002/nme.3374

Application of an elastoplastic spectral-element method to 3D slope stability analysis

Hom Nath Gharti[1,2,*,†], Dimitri Komatitsch[3,4], Volker Oye[1], Roland Martin [3] and Jeroen Tromp[5]

[1]*NORSAR, Gunnar Randers vei 15, N-2007 Kjeller, Norway*
[2]*Department of Geosciences, Oslo University, Sem Sælands vei 1, N-0371 Oslo, Norway*
[3]*Géosciences Environnement Toulouse CNRS UMR 5563, Observatoire Midi-Pyrénées (OMP), Université Paul Sabatier, 14 avenue Édouard Belin, 31400 Toulouse, France*
[4]*Institut universitaire de France, 103 boulevard Saint-Michel, 75005 Paris, France*
[5]*Department of Geosciences and Program in Applied and Computational Mathematics, Princeton University, Princeton, NJ 08544, USA*

SUMMARY

We implement a spectral-element method for 3D time-independent elastoplastic problems in geomechanics. As a first application, we use the method for slope stability analyses ranging from small to large scales. The implementation employs an element-by-element preconditioned conjugate-gradient solver for efficient storage. The program accommodates material heterogeneity and complex topography. Either simple or complex water table profiles may be used to assess effects of hydrostatic pressure. Both surface loading and pseudostatic seismic loading are implemented. For elastoplastic behavior of slopes to be simulated, a Mohr–Coulomb yield criterion is employed using an initial strain method (i.e., a viscoplastic algorithm). For large-scale problems, the software is parallelized on the basis of domain decomposition using Message Passing Interface. Strong-scaling measurements demonstrate that the parallelized software performs efficiently. We validate our spectral-element results against several other methods and apply the technique to simulate failure of an earthen embankment and a mountain slope. Copyright © 2012 John Wiley & Sons, Ltd.

Received 28 January 2011; Revised 21 October 2011; Accepted 25 October 2011

KEY WORDS: finite-element method; spectral-element method; elastoplasticity; 3D slope stability; pseudostatic seismic loading; parallel processing

1. INTRODUCTION

The finite-element method (FEM) is a powerful tool for solving boundary value problems. It is widely used in many areas of solid and fluid mechanics [1–3]. The flexibility of unstructured meshing based on a variety of element types (triangles, tetrahedra, hexahedra, shells, etc.) and the adaptability of using an arbitrary order of integration via Gaussian quadrature make the FEM a highly versatile tool. The spectral-element method (SEM) is a higher-order FEM. Unlike a classical FEM, however, the SEM employs nodal quadrature, namely Gauss–Legendre–Lobatto (GLL) quadrature. In nodal quadrature, interpolation nodes coincide with integration points. The coincidence of integration and interpolation points has two main advantages: (1) interpolation is unnecessary

*Correspondence to: Hom Nath Gharti, NORSAR, Gunnar Randers vei 15, N-2007 Kjeller, Norway.
[†]E-mail: homnath@norsar.no

to determine nodal quantities from quantities at quadrature points and vice versa, thus simplifying computation of the stiffness matrix, strain, stress, and so on; and (2) interpolating functions become orthogonal on quadrature points, resulting in a diagonal mass matrix, thereby simplifying the time-marching algorithm because a fully explicit scheme may be used [1]. Therefore, higher-order elements are easier to implement in the SEM. Nodal quadrature was originally limited to specific types of elements, for example, quadrilaterals in 2D and hexahedra in 3D. Hexahedral meshing is a challenging task and an area of active research [4–6]. Only a few hexahedral meshing tools are currently available, for example, CUBIT [7], TrueGrid [8], and GMSH [9]. Meshing is usually not fully automated, and careful mesh design is necessary. Recently, there have been some successful implementations of the SEM on other types of elements (e.g., triangles in 2D and tetrahedra in 3D), using so-called Fekete points [10–13]. Because nodal quadrature includes the end points of the integration interval, an n-point GLL quadrature is exact for polynomials of order $2n - 3$ [14]. Therefore, the order of integration may not always be sufficiently high [15]. Although the tradeoffs between high-spatial accuracy and low-order integration are not entirely clear, the influence of low-order integration on accuracy and convergence may not be significant, depending on the specifics of the problem [16, 17].

The SEM was originally developed to address problems in computational fluid dynamics [18, 19]. Detailed reviews may be found in, for example, Cohen [20] and Deville *et al.* [21]. Recently, the method has been widely used to simulate seismic wave propagation from local to global scales [22–29]. The nonlinear SEM has been used for 2D viscoplastic problems [30].

Several problems in geomechanics, for example, slope failure, and mine or tunnel collapse, may be described using elastoplastic deformation, which is an inherently nonlinear process. Such problems are usually solved using a higher-order nonlinear FEM [3, 31–36]. Because of the nonlinearity and the use of higher-order elements, computation is frequently demanding; therefore, the SEM may be a suitable tool for these problems.

Slope stability analysis is one of the important problems in geotechnical engineering, offering important guidelines for landslide hazard preparedness, and safe and economic design of infrastructures, such as dams and roads [37, 38]. Limit equilibrium method is probably the most widely used method for slope stability analysis [37, 39]. This method is based on the concept of equilibrium of a rigid body above an assumed failure surface. Therefore, the choice of failure surface is critical in this method. Two forces are assumed to act on the rigid body: a driving force that tries to move the body and a resisting force that prevents the slope from failing. The slope becomes unstable if the total driving force acting on the rigid body exceeds the resisting force, thereby breaking equilibrium. The ratio between resisting and driving forces for the potential failure surface is often referred to as the factor of safety (FOS). Computation has to be repeated for several assumed failure surfaces to determine the most critical failure surface. The actual forces are often estimated by dividing the rigid body into several pieces of a simpler geometry (e.g., vertical columns). There are several limit equilibrium methods, for example, the ordinary, modified Bishop, Morgenstern and Price, Spencer, and Janbu methods (details may be found in, e.g., Abramson *et al.* [37]), and there have been numerous improvements to these methods [40–44]. The limit equilibrium method is simple and fast. Unfortunately, it is very difficult to define a realistic failure surface for a complex model with material heterogeneity, particularly in 3D. In addition to the failure surface, assumptions have to be made regarding the side forces on the columns [45]. Limit analysis method based on the concept of yield design theory or limit theorems of plasticity is also used for the slope stability analysis [46–48]. The method gives the lower and upper bound estimates of the stability factor of the slope considering static and kinematic approaches, respectively. The lower bound solution is estimated considering a statically admissible stress field that does not violate the yield criterion in the entire domain [49, 50]. Similarly, the upper bound solution is estimated considering a kinematically admissible velocity field on the failure mass above an assumed failure surface, where the velocity and displacement fields obey the plastic flow rule [51, 52]. For simplicity, the material is generally assumed to be perfectly plastic with an associative flow rule. Optimization technique such as the linear or nonlinear programming has to be used to determine the critical FOS and corresponding failure surface [53, 54].

DOI: 10.1002/nme

Stress-deformation analysis is another method used for slope stability analysis. In this approach, a numerical method is used to compute the displacement field to simulate stress-deformation behavior of the slope. Despite the fact that this approach has a large computational burden, it offers several distinct advantages, namely no assumptions need to be made regarding a potential failure surface or side forces, and the progressive nature of slope failure may be captured because the displacement field is computed at each stage [55]. Because of the advent of modern computers, these methods are becoming increasingly popular. Methods based on this approach may be broadly classified into two main categories: (1) continuum modeling and (2) discontinuum modeling.

Continuum modeling describes the model as a continuous body. Therefore, this method is applicable to slopes whose behavior may be realistically reproduced under the continuum assumption, for example, soils, massive sound rock, and heavily jointed rock. Commonly used continuum-based methods for slope stability analysis are the FEM and the finite-difference method (FDM). Whereas the FEM solves a weak (variational) form of the governing equation on an unstructured mesh, the FDM solves a strong form, often on a structured grid [3, 56]. Discretization and the solution procedure are relatively simple in the FDM. However, it is often difficult to model complex geometries with a structured grid. Moreover, in the strong formulation, a separate equation for the traction-free boundary condition must be solved. On the contrary, unstructured meshing is well suited for complex geometries. In addition, in the weak formulation, traction-free boundary conditions are automatically satisfied [57]. Therefore, the FEM is capable of solving a wide range of problems in solid mechanics, and it generally gives more accurate results for complicated boundary geometries. The FEM has been applied to slope stability problems in 2D and 3D [58–62]. Some methods also combine the FEM with the limit equilibrium concept for faster and flexible stability analysis [63, 64], but a potential failure surface still has to be assumed. There are also a few studies of slope stability based on the FDM [65, 66].

Discontinuum modeling considers the model as an assemblage of discrete particles interacting through contact [67]. Commonly used methods are the distinct-element method, discontinuous deformation analysis, and particle flow codes. Collectively, these methods are referred to as discrete-element methods (DEMs). Originally, the DEM was proposed by Cundall [68, 69] for problems in rock mechanics. Since then, it has been used to address a number of problems, in particular for granular materials and blocky structures [70, 71]. It has also been used to study landslides, such as the Val Pola landslide [72], and seismic triggering of landslides in Kyrgyzstan [73]. The DEM has also been used to model catastrophic landslides, for example, the 1991 Randa rock slide in Switzerland [74], and mass flow avalanches due to the 1999 Chichi Earthquake in Taiwan [75, 76]. Most of these studies were performed in 2D, although there have been a few 3D investigations [77, 78]. Hybrid techniques have also been developed to couple the DEM and FEM [79–81]. Recently, the smooth particle hydrodynamics [82] has been applied for the slope stability analysis [83].

Although the particle-based methods are capable of simulating discontinuous models realistically, these methods require a large number of particles. Hence, these methods are often prohibitively expensive for large-scale problems. In this regard, special techniques, such as the extended FEM [84, 85] and the particle discretization scheme FEM [86, 87], are of interest. Recently, the extended FEM has been applied to detect soil instabilities in elastoplastic soils due to existing discontinuities [88]. These methods may be suitable for slopes, in which case discrete discontinuities or block structures are dominant. Nevertheless, continuum modeling is capable of addressing a wide range of slope stability problems.

Most existing tools for slope stability analysis are limited to either 2D or relatively simple and small 3D problems. In this article, we implement the SEM for 3D slope stability problems of various scales. As described earlier, the SEM is a continuum-based approach. Our SEM software can handle material heterogeneity and a complex model with significant topography. Both simple and complex free surface profiles may be used on the basis of a simple hydrostatic relation. We implement both surface loading and pseudostatic seismic loading. For efficient storage, we use an element-by-element preconditioned conjugate-gradient (PCG) method [89]. The program is parallelized on the basis of domain decomposition. We compare our results with classical FEM calculations and several limit-equilibrium-based methods, and apply the method to simulate failure of a reservoir embankment and slumping of a mountain slope.

DOI: 10.1002/nme

2. FORMULATION

2.1. Discretization of the governing equations

The governing equations for elastodynamics problems may be written in index notation as

$$\sigma_{ij;j} + f_i = \rho\, \ddot{u}_i, \tag{1}$$

where a dot over a symbol denotes partial differentiation with respect to time; $\sigma_{ij} = C_{ijk\ell}\, \varepsilon_{k\ell}$ represents the Cauchy stress tensor, $\varepsilon_{k\ell} = 1/2(u_{k;\ell} + u_{\ell;k})$ the small strain tensor, $C_{ijk\ell}$ the fourth-order tensor relating stress and strain, f_i the force term, ρ the mass density, and u_i and $\ddot{u}_i$ particle displacement and acceleration, respectively. We use the summation convention for repeated indices, and a semicolon (;) denotes covariant differentiation.

The weak form of the governing Equation (1) is

$$\int_\Omega \rho\, w_i\, \ddot{u}_i\, \mathrm{d}\Omega + \int_\Omega w_{i;j}\, \sigma_{ij}\, \mathrm{d}\Omega = \int_\Omega w_i\, f_i\, \mathrm{d}\Omega + \int_\Gamma w_i\, t_i\, \mathrm{d}\Gamma, \tag{2}$$

where w_i denotes a test function, $t_i = \sigma_{ij}\, \hat{n}_j$ the traction on the boundary, Ω and Γ the volume and boundary of the domain, respectively, and $\hat{n}_i$ the unit outward normal to the boundary.

Spectral-element discretization and integration techniques are explained in the literature [19–21, 24, 25, 27]. For completeness, we briefly summarize them here. In the SEM, the displacement field is expressed as

$$u_i(\boldsymbol{\xi}) = \sum_{\alpha=1}^{N} u_i^\alpha\, \phi^\alpha(\boldsymbol{\xi}), \tag{3}$$

where u_i^α and ϕ^α denote nodal displacements and interpolation functions, respectively. In each direction, $j = 1$, 2, or 3, in the natural state with coordinates $\boldsymbol{\xi} = \{\xi_j\}$, the $N_j = n + 1$ GLL interpolation points are the roots of $(1-\xi^2)\, P_n'(\xi) = 0$, where P_n denotes the Legendre polynomial of degree n. The total number of interpolation points is the product of the number of GLL points along each direction: $N = \prod_{j=1}^{3} N_j$. The interpolation functions ϕ^α in natural coordinates are determined by the tensor product of one-dimensional Lagrange polynomials,

$$\phi^\alpha(\boldsymbol{\xi}) = \prod_{j=1}^{3} \phi_j^{\alpha_j}(\xi_j), \tag{4}$$

such that

$$\phi_j^{\alpha_j}(\xi_j) = \prod_{\substack{\beta=1 \\ \beta\neq\alpha_j}}^{N_j} \frac{(\xi_j - \xi_j^\beta)}{(\xi_j^{\alpha_j} - \xi_j^\beta)}, \tag{5}$$

where α is the index of a GLL point located at $\{\alpha_1, \alpha_2, \alpha_3\}$, given for instance by $\alpha = N_1 N_2(\alpha_3 - 1) + N_1(\alpha_2 - 1) + \alpha_1$ using a 3D to 1D linear mapping.

For numerical integration, a point $\mathbf{x} = \{x_i\}$ in a deformed element is mapped to a point $\boldsymbol{\xi} = \{\xi_j\}$ in the natural element, as illustrated in Figure 1, using the transformation

$$\mathbf{x}(\boldsymbol{\xi}) = \sum_{\alpha=1}^{N_\mathrm{g}} \mathbf{x}^\alpha\, \psi^\alpha(\boldsymbol{\xi}). \tag{6}$$

Here, ψ^α denotes a shape function and N_g the number of geometrical nodes $\mathbf{x}^\alpha$ of an element. The Jacobian matrix of the transformation has elements given by $J_{ij}(\boldsymbol{\xi}) = \partial x_i(\boldsymbol{\xi})/\partial \xi_j$. The same GLL points are used as quadrature points for numerical integration.

Because the internal GLL points of a spectral element do not contribute to the inter-element connectivity, these points can safely be excluded during interpolation of the model geometry, that

DOI: 10.1002/nme

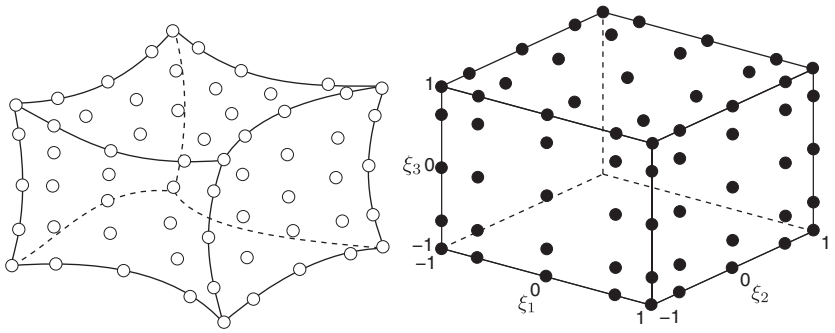

Figure 1. (a) A typical spectral element with five interpolation nodes (open circles) in each dimension. (b) The same spectral element mapped to its natural coordinates. The Gauss–Legendre–Lobatto points (solid black circles) are used for numerical integration. Integration points and interpolation nodes coincide. Only interpolation nodes on the three visible faces are shown for clarity.

is, N and N_g may be different. Therefore, the shape functions ψ^α for transformation (6) should be chosen carefully because we cannot always determine these from tensor products similar to Equation (4). Depending on element type and numerical algorithm, fewer points may be sufficient to capture transformation (6). For example, for a planar faceted hexahedral element, only the eight corner nodes are required to capture the geometry if the deformed mesh is not relevant for further simulations, for example, strain-displacement matrix (so-called B matrix) computation. Therefore, we usually have $N > N_g$, and consequently, the degree of the interpolating functions, ϕ^α, is greater than the degree of the shape functions, ψ^α, leading to a subparametric formulation.

The SEM is a continuous Galerkin method, in which the interpolation function ϕ^α is taken as the test function w_i. Upon substituting $w_i = \phi^\alpha$ and u_i, given by Equation (3), in Equation (2), we obtain a set of elemental equations that may be written conveniently in the matrix–vector form

$$\mathbf{M}_e\ddot{\mathbf{U}}_e + \mathbf{K}_e\mathbf{U}_e = \mathbf{F}_e, \tag{7}$$

where $\mathbf{M}_e$, $\mathbf{K}_e$, and $\mathbf{F}_e$ are known as the mass matrix, stiffness matrix, and force vector of an element, respectively. Similarly, $\ddot{\mathbf{U}}_e$ and $\mathbf{U}_e$ are the acceleration and displacement vectors, respectively. Symbolically, we write

$$\mathbf{M}_e = \int_{\Omega_e} \rho\,\mathbf{\Phi}^T\mathbf{\Phi}\,\mathrm{d}\Omega, \quad \mathbf{K}_e = \int_{\Omega_e} \mathbf{B}^T\,\mathbf{C}\,\mathbf{B}\,\mathrm{d}\Omega, \quad \mathbf{F}_e = \int_{\Omega_e} \mathbf{\Phi}^T\,\mathbf{f}\,\mathrm{d}\Omega + \int_{\Gamma_e} \mathbf{\Phi}^T\,\mathbf{t}\,\mathrm{d}\Gamma, \tag{8}$$

where a superscript T denotes the transpose and Ω_e the volume of an element. The quantities Φ, $\mathbf{B}$, and $\mathbf{C}$ are known as the interpolation function matrix, the strain-displacement matrix, and the elasticity matrix, respectively. More specifically, the elemental mass matrix in Equation (8) is determined by

$$M_e^{\alpha\beta} = \int_{\Omega_e} \rho(\mathbf{x})\,\phi^\alpha(\mathbf{x})\,\phi^\beta(\mathbf{x})\,\mathrm{d}\Omega, \tag{9}$$

where $\alpha, \beta = 1, \ldots, N$. Using numerical integration based on GLL quadrature over the GLL points, we obtain

$$M_e^{\alpha\beta} \approx \sum_{\gamma=1}^{N} w^\gamma \rho(\boldsymbol{\xi}^\gamma)\,\phi^\alpha(\boldsymbol{\xi}^\gamma)\,\phi^\beta(\boldsymbol{\xi}^\gamma)\,J(\boldsymbol{\xi}^\gamma), \tag{10}$$

where w^γ and $J(\boldsymbol{\xi}^\gamma)$ are, respectively, the integration weights and the determinant of the Jacobian matrix evaluated at the γth integration point. Using the orthogonality of the interpolation functions,

DOI: 10.1002/nme

we obtain

$$M_e^{\alpha\beta} \approx \sum_{\gamma=1}^{N} w^{\gamma}\, \rho(\boldsymbol{\xi}^{\gamma})\, \delta^{\alpha\gamma}\, \delta^{\beta\gamma}\, J(\boldsymbol{\xi}^{\gamma}) = \delta^{\alpha\beta} \sum_{\gamma=1}^{N} w^{\gamma}\, \rho(\boldsymbol{\xi}^{\gamma})\, J(\boldsymbol{\xi}^{\gamma}), \tag{11}$$

where $\delta^{\alpha\beta}$ is the Kronecker delta. Therefore, the elemental mass matrix is diagonal, which is also true for the global mass matrix. This facilitates an efficient time-marching scheme, which is a significant advantage of the SEM over the classical FEM.

Upon assembling the elemental equations, we obtain a set of global equations

$$\mathbf{M}\,\ddot{\mathbf{U}} + \mathbf{K}\,\mathbf{U} = \mathbf{F}. \tag{12}$$

In this article, we deal only with time-independent elastoplastic problems relevant to slope stability analysis, such that

$$\mathbf{K}\,\mathbf{U} = \mathbf{F}. \tag{13}$$

Thus, the SEM advantage of a diagonal mass matrix is irrelevant for static slope stability problems, but we shall see that the SEM still offers benefits over the classical FEM.

2.2. External loading

We consider three different slope loads: gravity loading, surface traction, and pseudostatic seismic loading. Gravity loading is caused by the self weight of the slope and can be considered as a body load. It is computed using the volume integral

$$(\mathbf{F}^{\mathrm{gr}})_e = \int_{\Omega_e} \boldsymbol{\Phi}^T\, \mathbf{f}^{\mathrm{gr}}\, \mathrm{d}\Omega, \tag{14}$$

where $\mathbf{f}^{\mathrm{gr}}$ is the gravity force per unit volume. In our case, the gravity force always acts downward in the vertical direction, that is, $\mathbf{f}^{\mathrm{gr}} = \{0, 0, -\gamma_e\}$, where γ_e is the unit weight of slope material on the eth element. Although, most slope failures are considered to be gravity driven, in some cases, it may be important to include the initial stress state [90]. The initial stress state of slopes mainly depends on the geological structure and loading history, and it may be implemented as a body load in the SEM.

Similarly, the load due to surface traction is computed using the surface integral

$$(\mathbf{F}^{\mathrm{tr}})_e = \int_{\Gamma_e} \boldsymbol{\Phi}^T\, \mathbf{t}\, \mathrm{d}\Gamma. \tag{15}$$

To numerically calculate this integral, it is often convenient to define interpolation and shape functions in 2D. These functions may be computed analogous to Equations (4) and (6) but considering a quadrilateral element. In that case, the 2D Jacobian is given by $J(\xi_1, \xi_2) = \|\partial_{\xi_1}\mathbf{x} \times \partial_{\xi_2}\mathbf{x}\|$.

Slope stability under earthquakes is often analyzed using a pseudostatic approach, in which the effects of an earthquake are represented by constant horizontal and/or vertical accelerations [91,92]. These accelerations are used to determine the pseudostatic load applied to the slope. Therefore, the pseudostatic seismic load may be computed using the volume integral

$$(\mathbf{F}^{\mathrm{eq}})_e = \gamma_e \int_{\Omega_e} \boldsymbol{\Phi}^T\, \mathbf{k}^{\mathrm{eq}}\, \mathrm{d}\Omega, \tag{16}$$

where $\mathbf{k}^{\mathrm{eq}}$ denotes the pseudostatic earthquake coefficient, which may be expressed as the ratio of pseudostatic to gravitational accelerations. The vertical pseudostatic force has minimal influence on stability; therefore, only a horizontal pseudostatic coefficient ($k_{\mathrm{h}} = k_1 = k_2$) is considered. The direction of pseudostatic seismic loading is chosen such that it gives the worst condition for stability. The approach of expressing earthquake loading by pseudostatic forces was originally proposed by Terzaghi [93], who suggested a value of k_{h} equal to 0.1 for severe earthquakes, 0.2 for violent

DOI: 10.1002/nme

earthquakes, and 0.5 for catastrophic earthquakes. Several authors have suggested alternative pseudostatic coefficients depending on the problem [94, 95]. It should be noted that the pseudostatic approach is an approximate procedure, and it cannot reproduce actual behavior under cyclic earthquake loading. Sometimes, it may even give misleading results [96, 97]. Nevertheless, this approach offers several advantages: it is simple and straightforward, it can be implemented easily in both limit equilibrium and stress-deformation approaches, and it gives a quantitative value that may be important for the qualitative analysis of earthquake hazard [91]. Dynamic slope stability analysis may be performed on the basis of the SEM by considering an appropriate cyclic constitutive model and actual earthquake loading; this will be of future interest.

2.3. Elastoplastic failure

For elastoplastic slope deformation, we implement a Mohr–Coulomb yield criterion considering an elastic-perfectly plastic and non-associative material. Some other commonly used criteria, such as Tresca, Huber-von Mises, and Drücker-Prager [3], have relatively simpler yield surfaces with fairly straightforward implementations. For complex models, such as the critical state family [98], some modifications may be necessary. The Mohr–Coulomb yield criterion may be expressed as

$$F = \sigma_{\mathrm{m}} \sin\phi' + \bar{\sigma} \left(\cos\theta - \frac{1}{\sqrt{3}} \sin\phi' \sin\theta \right) - c' \cos\phi', \tag{17}$$

where c' and ϕ' represent the effective cohesive strength and internal friction angle of the material, and σ_{m}, $\bar{\sigma}$, and θ are the stress invariants known as the mean stress, deviatoric stress, and Lode angle, respectively. The stress invariants are computed using the effective stress, which is obtained using the relation

$$\sigma'_{ij} = \sigma_{ij} - p\,\delta_{ij}, \tag{18}$$

where p denotes water pressure. A rigorous way of computing p would be to determine the flownet depending on permeability and appropriate seepage conditions [3, 99]; however, for slope stability problems, it is often considered sufficient and conservative [45] to approximate pressure with the simple hydrostatic relation $p = \gamma_{\mathrm{w}}\, h_{\mathrm{w}}$, where γ_{w} denotes the unit weight of water and h_{w} the depth of the water column.

We solve the elastoplastic problem in an iterative manner using the initial strain method (also called the viscoplastic algorithm [100, 101]). The global equations are solved using a constant stiffness approach, which attempts to satisfy nonlinear behavior by iteratively correcting the loads and solving the linear system at each iteration [102], namely

$$\mathbf{K}\,\mathbf{U}^k = \mathbf{F} + (\mathbf{F}^{\mathrm{p}})^{k-1}. \tag{19}$$

The force term, $\mathbf{F}^{\mathrm{p}}$ at the kth iteration, depends on the incremental plastic strain, $\delta\boldsymbol{\varepsilon}^{\mathrm{p}}$, and is given by

$$(\mathbf{F}^{\mathrm{p}})^k = (\mathbf{F}^{\mathrm{p}})^{k-1} + \sum_{\text{elements}} \int_{\Omega_e} \mathbf{B}^T\,\mathbf{C}\,(\delta\boldsymbol{\varepsilon}^{\mathrm{p}})^k \,\mathrm{d}\Omega. \tag{20}$$

The force contributed by the incremental plastic strain is self-equilibrating so that the net loading remains the same. This load is accumulated in successive iterations until convergence is achieved. In our numerical implementation, we use the maximum norm of the difference in displacements between two successive iterations as the convergence criterion.

3. PARALLEL IMPLEMENTATION

The program is parallelized on the basis of a non-overlapping domain decomposition method in which each domain contains a unique set of elements; no domains share elements, and only nodes on common domain interfaces are shared. The Message Passing Interface is used as the parallel

DOI: 10.1002/nme

library [103, 104]. For efficient parallel processing, the number of elements should be approximately divided equally among domains, and the number of nodes on domain interfaces should be minimal. Therefore, efficient mesh partitioning is required. There are a few open-source tools for mesh partitioning, for example, SCOTCH [105, 106] and METIS [107].

To solve the system of linear equations, we use a parallel PCG method, which is an iterative solver widely used in the classical FEM. This approach has also been implemented in both overlapping and non-overlapping domain decomposition methods on distributed memory systems [108–110]. In the domain decomposition method, each processor solves its own part of the system, occasionally communicating across processors to assemble entities along common interfaces. For more details, we present the parallel algorithm of the PCG in Algorithm 1.

$\mathbf{r}_0 := \mathbf{F} - \mathbf{K}\,\hat{\mathbf{U}}_0$; $\quad \mathbf{z}_0 := \hat{\mathbf{D}}^{-1}\,\mathbf{r}_0$; $\quad \mathbf{p}_0 := \mathbf{z}_0$

for $k = 0$ to MAX_ITERATIONS **do**

$\alpha_k := \frac{\mathbf{r}_k^T\,\hat{\mathbf{z}}_k}{\hat{\mathbf{p}}_k^T\,\mathbf{K}\,\hat{\mathbf{p}}_k}$

$\hat{\mathbf{U}}_{k+1} := \hat{\mathbf{U}}_k + \alpha_k\,\hat{\mathbf{p}}_k$

if $\frac{\|\alpha_k\,\hat{\mathbf{p}}_\mathbf{k}\|_\infty}{\|\hat{\mathbf{U}}_{k+1}\|_\infty} \leq$ TOLERANCE **return**

$\mathbf{r}_{k+1} := \mathbf{r}_k - \alpha_k\,\mathbf{K}\,\hat{\mathbf{p}}_k$

$\mathbf{z}_{k+1} := \hat{\mathbf{D}}^{-1}\,\mathbf{r}_{k+1}$

$\beta_k := \frac{\mathbf{r}_{k+1}^T\,\hat{\mathbf{z}}_{k+1}}{\mathbf{r}_k^T\,\hat{\mathbf{z}}_k}$

$\mathbf{p}_{k+1} := \mathbf{z}_{k+1} + \beta_k\,\mathbf{p}_k$

end for

non-convergence

Algorithm 1: Parallel preconditioned conjugate-gradient method to solve the system $\mathbf{KU} = \mathbf{F}$. The preconditioner is represented by $\mathbf{D}$.

For simplicity, we use a Jacobi preconditioner, that is, $\mathbf{D} = \text{diag}(\mathbf{K})$. All hatted quantities in Algorithm 1 represent the local part of the corresponding assembled (global) quantities. The matrix–vector multiplication $\mathbf{K}\,\hat{\mathbf{p}}$ may be performed on an element-by-element basis [89], never forming a global stiffness matrix as given by relation (21). This strategy prevents storage of large arrays. Specifically,

$$\mathbf{K}\,\hat{\mathbf{p}} = \sum_{\text{elements}} \mathbf{K}_e\,\hat{\mathbf{p}}_e, \tag{21}$$

where $\mathbf{K}_e$ and $\hat{\mathbf{p}}_e$ are the elemental matrix and vector expanded to the same size as $\mathbf{K}$ and $\hat{\mathbf{p}}$, respectively, but having entries only in locations corresponding to the eth element. In practice, neither $\mathbf{K}_e$ nor $\hat{\mathbf{p}}_e$ need be expanded. Only the elemental entries are scattered to their respective locations of the composite vector.

The stiffness matrix never needs to be assembled along common interfaces; only certain vectors need to be assembled. We only need one assemblage of vector $\mathbf{D}$ outside the PCG loop (Algorithm 1), and only two vectors, $\mathbf{z}$ and $\mathbf{p}$, need to be assembled inside the loop. The scalar

DOI: 10.1002/nme

variables α, β, and L^∞-norms (i.e., $\|\alpha_k\,\hat{\mathbf{p}}_\mathbf{k}\|_\infty$ and $\|\hat{\mathbf{U}}_{k+1}\|_\infty$) have the same values across processors. Two L^∞-norms and four dot products involved in the numerator and denominator of α and β involve global operations. Each requires the communication of a scalar value across processors. For faster convergence, we may use the displacement field obtained in the previous nonlinear iteration as the initial guess ($\hat{\mathbf{U}}_\mathbf{0}$) for the conjugate-gradient solver. In the future, other algorithms that provide data locality, for example, localized ILU preconditioning [111], will be of interest.

4. NUMERICAL RESULTS

4.1. Validation

To validate the method, we first apply it to predict a FOS and potential failure surface of a given model. To determine the FOS, we use the shear strength reduction technique [59, 112], in which the strength parameters c' and ϕ' are reduced by a certain reduction factor as

$$c'_\mathrm{f} = \frac{c'}{\mathrm{SRF}}, \quad \phi'_\mathrm{f} = \arctan\left(\frac{\tan\phi'}{\mathrm{SRF}}\right), \tag{22}$$

where SRF is a strength reduction factor. The value of the SRF is increased repeatedly until the slope fails, thereby identifying the FOS of the slope. To identify the failure stage, we plot the maximum displacement against SRF. The SRF at which we observe a sudden increment in displacement gives the FOS [113]. As failure approaches, more Gauss points undergo plastic deformation, requiring a large number of iterations for convergence. Therefore, nonconvergence within a predefined limit may also be used to identify failure [3]. We should note that convergence is dependent on error tolerance, maximum number of iterations (iteration ceiling), and sometimes problem size. Therefore, some tests may be necessary to determine the iteration ceiling for nonconvergence. There are several other procedures to identify failure, for example, tests on slope bulging [114], limiting shear stress on the potential failure surface [115], the total equivalent plastic strain zone [116], the ratio of unbalanced force to applied loading [117], or formulation of an initial value problem to trace the critical slide line [118]. Zheng *et al.* [118] suggested forcing a so-called $\phi - \nu$ inequality (i.e., friction angle and Poisson's ratio inequality), namely $\sin\phi \geqslant 1 - 2\,\nu$ during strength reduction, to obtain a more reliable plastic zone. Similarly, Duan *et al.* [119] suggested adjusting Young's modulus (E) and Poisson's ratio (ν) simultaneously. Some authors reported that the elasticity parameters (i.e., ν and E) have little influence on slope stability [117, 120], but contrary results have also been reported [63]. Although stress-deformation approaches (FEM, SEM, etc.) are well suited for studying the $\phi - \nu$ inequality or the influence of elasticity parameters, we do not adjust elasticity parameters during strength reduction in our examples. The influence of such adjustments and elasticity parameters on slope stability will be of future interest.

For validation purposes, we compute the FOS and potential failure surface for the model shown in Figure 2, which consists of a weak layer and water table, closely resembling a realistic field problem. The weak layer may be interpreted as a geosynthetic layer or a discontinuity. This model was originally used in 2D by Fredlund and Krahn [121] and later extended to 3D by Xing [41]. Since then, several authors have used it as a benchmark for validating their methods [42, 51, 55, 64]. To test the robustness of our method, we consider four different cases motivated by the original problem as follows:

Case 1. Homogeneous dry slope.
Case 2. Dry slope with a weak layer.
Case 3. Partially wet slope with a weak layer (original model).
Case 4. Partially wet slope with a weak layer and pseudostatic seismic loading.

We compute the displacement field for several SRFs with three different programs: (1) a FEM adapted from Smith and Griffiths [101]; (2) our serial SEM; and (3) our parallel SEM. In the FEM, we use 20-node hexahedral elements with four Gauss points for numerical integration. This is a reduced integration, which is usually used to prevent the so-called 'locking' phenomenon [3, 101]. The FEM package [101] we currently have cannot handle the water table or pseudostatic seismic

DOI: 10.1002/nme

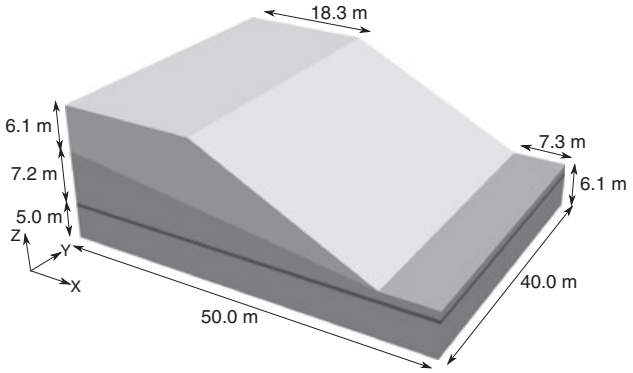

Figure 2. Slope model used for validation: dry region (light gray), wet region (dark gray), and 0.5 m thick weak layer (black). Top surfaces of the wet region mark the water table. The dry and wet regions have the same material properties of unit weight $\gamma = 18.8$ kN/m^3, friction angle $\phi = 20^0$, and cohesion $c = 29$ kN/m^2. The weak layer has material properties of $\gamma = 18.8$ kN/m^3, $\phi = 0^0$, and $c = 10$ kN/m^2. The dilation angle, Young's modulus, and Poisson's ratio are taken, respectively, as 0, 10^5 kN/m^2, and 0.3 for both regions.

loading. Therefore, we use the FEM only for the first two cases. For both the serial and parallel SEMs, we use 3, 4, or 5 GLL points in each direction, that is, the number of nodes per element is 27, 64 or 125. Because the model is symmetric about the xz-plane, we take advantage of this symmetry and solve only for the symmetric half of the model using appropriate boundary conditions on the symmetry plane. For the boundary conditions, the left and right faces are partially constrained along the x-axis. Similarly, the front and bottom faces are fully constrained, whereas the symmetry face is partially constrained only along the y-axis.

To mesh the model, we use the mesh generation toolkit CUBIT developed by Sandia National Laboratory [7]. For the FEM, 20-node hexahedral elements may be created directly within CUBIT (Figure 3a). However, creating spectral elements with different GLL nodes is currently not possible within CUBIT. Therefore, first we create eight-node hexahedral elements with CUBIT; subsequently, in the SEM program, spectral elements with the desired number of nodes are created on the basis of the GLL points (Figure 3b). If necessary, spectral elements may also be created using any type of hexahedral element of higher degree. For the parallel SEM implementation, meshes are partitioned using SCOTCH [105] (Figure 3c). We use a relative tolerance of 10^{-8} for conjugate-gradient iterations and 5×10^{-4} for nonlinear iterations.

Case 1: Homogeneous dry slope. This is the simplest model, involving a homogeneous material. The gravity load caused by self weight is the only load acting on the slope. The meshes for the FEM, serial SEM, and parallel SEM are shown in Figure 3a–c. Each mesh consists of 1670 elements with an average size of 2 m; in the SEM, the number of GLL points in each direction is 3. For the parallel SEM, the mesh is partitioned into eight subdomains. Figure 4 shows the maximum displacement computed at various SRFs, and Figure 5a–b show the required total number of nonlinear plastic iterations and conjugate-gradient iterations. Initially, we observe small displacements until the reduction factor reaches approximately 2.0. Up to this value, the model behaves largely as an elastic material, and the three different results accurately match. Only a few iterations are required to converge to the solution. At a factor of approximately 2.18, the displacement suddenly increases and the curve becomes almost vertical, indicating possible slope collapse. A large part of the model undergoes plastic deformation, and the number of iterations required to achieve convergence sharply increases. We define this value as the FOS of this slope. As expected, the results for the serial and parallel SEMs perfectly coincide in terms of both displacements and required iterations. After collapse initiation, although displacements computed by the FEM and SEM are slightly different, the discrepancy between the estimated FOSs is negligible. Regarding the computational cost, the FEM and SEM require roughly the same number of iterations before collapse begins, although the FEM

DOI: 10.1002/nme

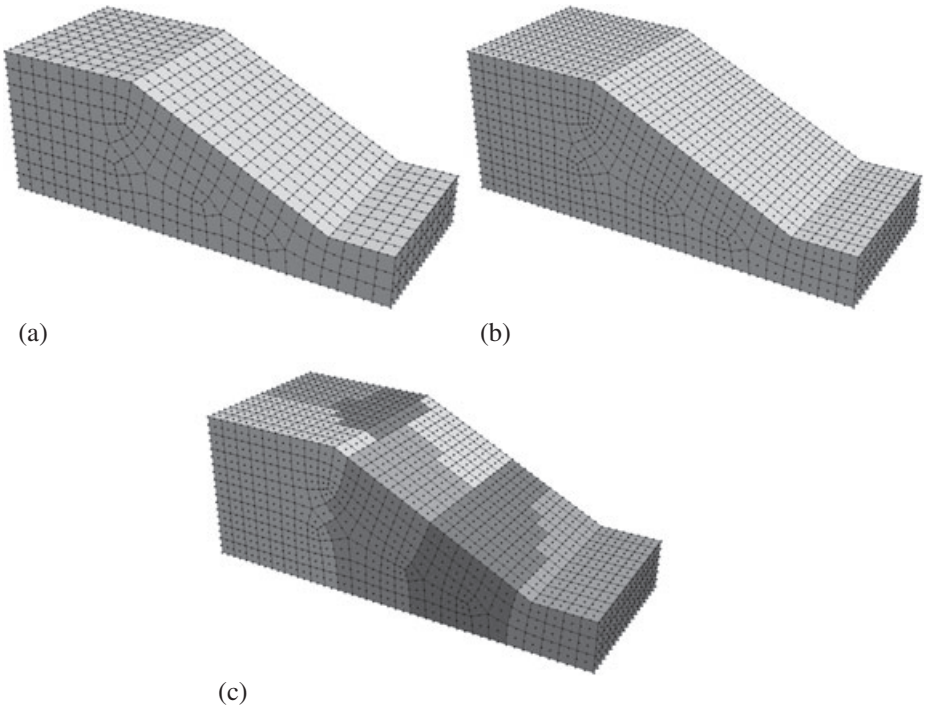

Figure 3. (a) Finite-element mesh of the symmetric half of the model with 20-node hexahedral elements. (b) Spectral-element mesh of the symmetric half of the model with 3 GLL points in each spatial direction. (c) Same as (b) but partitioned into eight domains for parallel processing. The total number of elements in all cases is 1670.

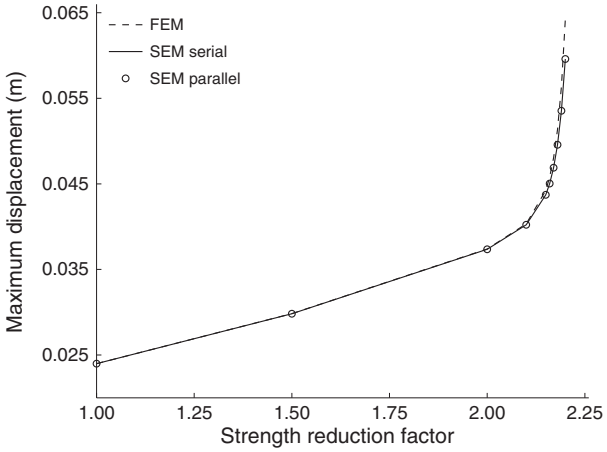

Figure 4. Maximum displacement at various strength reduction factors for Case 1. FEM, finite-element method; SEM, spectral-element method.

always requires a slightly larger number of iterations. But after collapse initiation, the number of iterations required for the FEM is noticeably higher than for the SEM, which may be significant for large-scale problem. In Table I, we compare the estimated FOS with results obtained by other authors. All methods except the FEM (Griffiths and Marquez [55]) in Table I are limit-equilibrium-based methods. As mentioned in Section 1, these methods are simple and fast, but they do not provide detail information on failure mechanism. Our FOS results are in good agreement. Despite using only 3 GLL points, we obtain fairly accurate results.

The resulting failure patterns are plotted in Figure 6a–b, illustrating possible failure mechanisms. We observe similar patterns for the FEM and SEM. We observe almost a circular failure mechanism,

DOI: 10.1002/nme

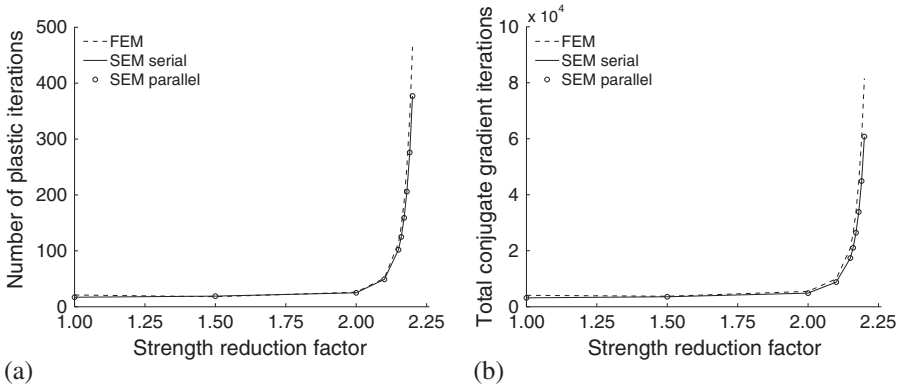

Figure 5. (a) Total number of plastic iterations and (b) total number of conjugate-gradient iterations required at various strength reduction factors for Case 1. FEM, finite-element method; SEM, spectral-element method.

Table I. Comparison of factor of safety obtained by different methods.

	Case 1	Case 2	Case 3	Case 4
Xing [41]	2.122	1.553	1.441	–
Bishop's modified method (Lam and Fredlund [42])	–	1.607	1.511	–
Janbu's simplified method (Lam and Fredlund [42])	–	1.558	1.481	–
CLARA (Lam and Fredlund [42])	–	1.62	1.54	–
GLE (Lam and Fredlund [42])	–	1.603	1.508	–
Chen *et al.* [51]	2.262	1.717	–	–
Chen *et al.* [64]	2.187	1.603	–	–
FEM (Griffiths and Marquez [55])	2.17	1.58	–	–
FEM	2.18	1.57	–	–
SEM	2.18	1.57	1.49	1.16

The serial and parallel spectral-element methods give identical results. GLE, general limit equilibrium; FEM, finite-element method; SEM, spectral-element method.

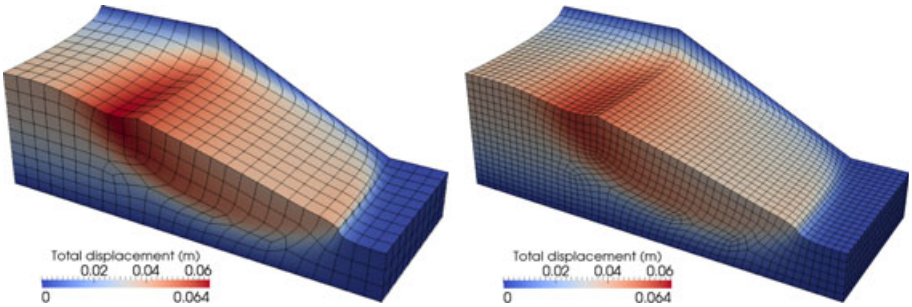

Figure 6. Deformed volume at failure for Case 1. (a) Finite-element method (FEM). (b) Serial spectral-element method (SEM). The results obtained by serial and parallel SEMs were identical. Actual deformation is increased along the displacement vector for clearer visualization. For FEM data visualization, 20-node hexahedral elements are used, whereas for the SEM, each hexahedral element is decomposed into $(N_1 - 1)(N_2 - 1)(N_3 - 1)$ eight-node hexahedra.

which appears quite realistic for the homogeneous model. Although, we used the same element size in both the FEM and SEM, the SEM figure appears to have higher resolution because of a visualization issue. We are able to render 20-node hexahedra directly, but we need to decompose each 27-node hexahedron into eight 8-node hexahedra to be able to visualize it with the graphics package that we use.

DOI: 10.1002/nme

Using the same model, we analyze convergence of the SEM with h-refinement (refining the mesh) and p-refinement (increasing the degree of interpolation) as compared with h-refinement in the FEM. For the FEM, we perform three complementary computations with three different mesh sizes. For the SEM, we first perform three computations with three different mesh sizes, keeping the number of GLL points fixed at 3. Next, we perform three SEM computations in which we vary the number of GLL points from 3 to 4 to 5, keeping both the number of elements and the mesh size constant. The results of these calculations are summarized in Figure 7a–b. Before collapse begins, we observe almost the same maximum displacements in all cases. After collapse, we observe discrepancies between results obtained with different degrees of h-refinement and p-refinement, but they all basically converge to the same FOS solution; the maximum discrepancy in the FOS is less than 1%. Griffiths and Marquez [55] performed a similar convergence test for their FEM implementation and found that the FOS discrepancy never exceeded 2%.

Mesh sizes of 1 and 0.075 m result in, respectively, 8 and 22 times more elements than a 2 m mesh size. The results obtained using 4 and 5 GLL points with a 2 m mesh size (p-refinement) are even better than the corresponding h-refinement results. Therefore, the SEM is a very accurate method, which may be important for other elastoplastic problems in geomechanics. However, in the context of slope stability, if the FOS is more important than the actual displacements, 3 GLL points are sufficient, facilitating faster simulations.

In h-refinement and p-refinement, the model is more densely sampled, leading to more accurate results. However, it is interesting to see how p-refinement influences results for the same number of discretization points (spectral nodes). In practice, it is very difficult to retain the same number of spectral nodes with varying polynomial degree. Using the same model as previously mentioned, we consider three different discretization schemes: (1) 3 GLL points with 1670 elements; (2) 4 GLL points with 511 elements; and (3) 5 GLL points with 220 elements. These three schemes correspond to 15,393, 15,862, and 16,233 spectral nodes, respectively, with a maximum variation of 5%. We summarize the results in Figure 8a–b. Although we observe significant discrepancies in displacements, particularly at failure, the influence on the FOS is negligible. As expected, higher-order elements are capable of capturing nonlinear behavior more accurately than lower order elements. Obviously, we obtain more accurate displacement fields using 220 elements and 5 GLL points than 1670 elements and 3 GLL points; however, because of the highly nonlinear behavior, the former requires more plastic iterations than the latter, thereby increasing the computational burden.

Our convergence tests show that 3 GLL points may be sufficient for prediction of the FOS and the potential failure surface. Therefore, we use 3 GLL points for the remaining three cases.

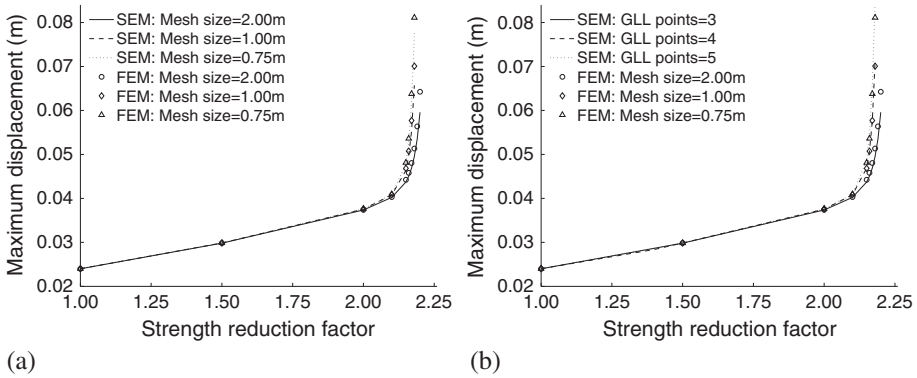

Figure 7. Maximum displacements at various strength reduction factors for Case 1. (a) Finite-element method (FEM) and spectral-element method (SEM) simulations with different mesh sizes. The total numbers of elements for mesh sizes of 2, 1, and 0.75 m (h-refinement) are 1670, 13,240, and 37,233, respectively. The SEM simulations for mesh sizes of 1 and 0.075 m were run on 16 and 24 processors, respectively. (b) FEM simulations with different mesh sizes and SEM simulations with varying number of Gauss–Legendre–Lobatto points (p-refinement). For the SEM simulations, the mesh size is 2 m.

DOI: 10.1002/nme

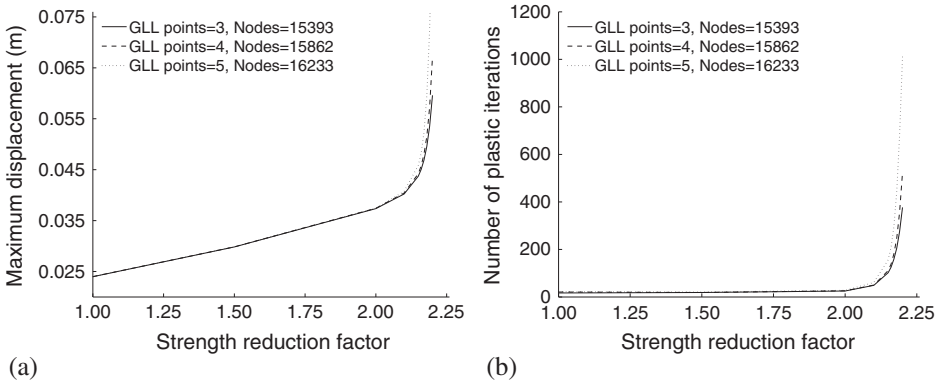

Figure 8. (a) Maximum displacement at various strength reduction factors and (b) number of plastic iterations for three different discretization schemes. The total number of spectral nodes is roughly the same in each case, the maximum variation being about 5%. GLL, Gauss–Legendre–Lobatto.

Case 2: Dry slope with a weak layer. In this test, we add a weak layer to the model in Case 1. Again the only load acting on the slope is gravity. The FEM and SEM meshes are shown in Figure 9a–b. Each mesh consists of 1890 elements with an average size of 2 m. However, the elements in the weak layer are smaller along the vertical axis. We obtain excellent agreement between the FEM, serial SEM, and parallel SEM (Figure 10). We estimate the value of the FOS to be about 1.57, which is in agreement with results obtained by other authors (Table I), including simulations based on CLARA [122] and the general limit equilibrium method by Lam and Fredlund [42]. In the presence of a weak layer, the FOS decreases significantly by about 28%. In comparison with the previous case, we observe interesting failure patterns (Figure 11a–b), illustrating that the slope fails along the weak layer. Both the FEM and SEM simulations show a similar failure pattern.

Case 3: Partially wet slope with a weak layer (original model). In this test, we add a water table to the model in Case 2, that is, we test the original model as shown in Figure 2. There is a gravity load acting on the slope. Additionally, water pressure acts on the wet region of the slope. The mesh for the SEM is shown in Figure 12a. Each mesh consists of 1800 elements with an average size of 2 m, although it is denser in the weak layer and around the sharp corners of the model. We use homogeneous material properties above and below the water table, which is honored by the mesh. Honoring the water table makes it easier to identify submerged nodes during the calculation of hydrostatic pressure, but it may adversely affect mesh quality, for example, around sharp corners (Figure 12a). Figure 12b shows the pressure distribution due to the water table.

Figure 10 illustrates that we obtain a perfect match between the serial and parallel SEMs (eight processors). As mentioned earlier, we cannot use our FEM package for this case. We estimate the

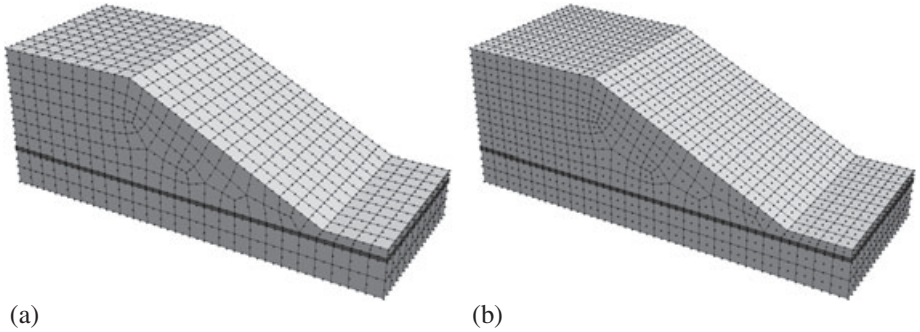

Figure 9. Mesh for a dry slope with a weak layer (Case 2): (a) finite-element method and (b) spectral-element method. The weak layer is shown in black.

DOI: 10.1002/nme

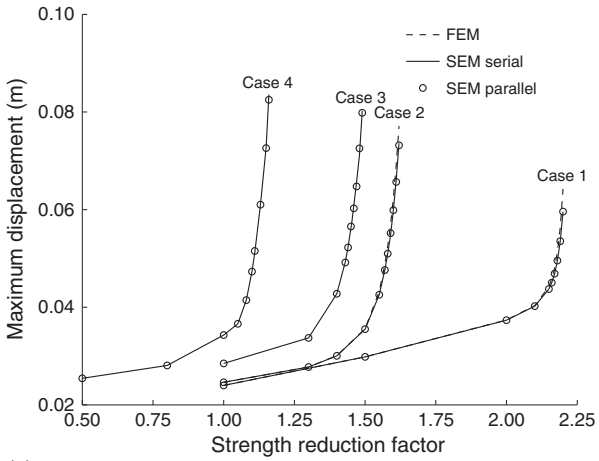

Figure 10. Maximum displacement at various strength reduction factors for four different cases. FEM, finite-element method; SEM, spectral-element method.

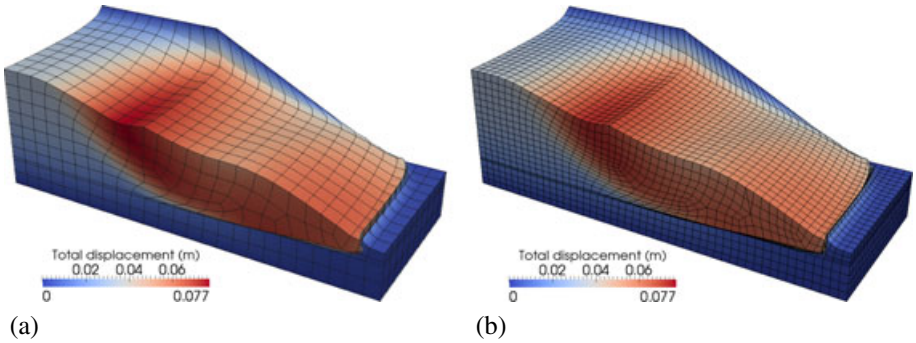

Figure 11. Deformed volume at failure for Case 2: (a) finite-element method and (b) serial spectral-element method. The results obtained by serial and parallel spectral-element methods were identical. Actual deformation is increased along the displacement vector for clearer visualization.

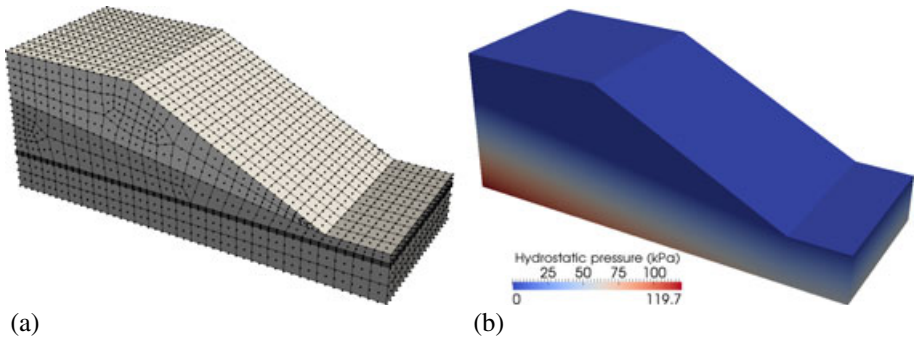

Figure 12. (a) Spectral-element method mesh for a dry slope with a weak layer and a water table (Cases 3 and 4). The weak layer is shown in black, and the wet region is shown in dark gray. (b) Hydrostatic pressure due to the water table.

value of the FOS to be approximately 1.49, which is a 5% reduction compared with Case 2 and a 32% reduction compared with Case 1. This suggests that the presence of a water table in some slopes will significantly reduce the FOS. Our FOS estimate is in close agreement with results obtained by other authors (Table I). The failure pattern (Figure 13a) again follows the weak layer, but the volume of failure is larger than in Case 2.

DOI: 10.1002/nme

Case 4: Partially wet slope with a weak layer and pseudostatic seismic loading. We now add a pseudostatic seismic load with a coefficient $k_h = 0.1$ to Case 3. Therefore, in addition to gravity and water pressure, an earthquake load acts on the slope. Because the model is constrained along the y-axis, the pseudostatic force will not have much significance along that direction. Similarly, the slope is oriented toward the positive x-axis; therefore, the worst effect is obtained if we apply the pseudostatic force along the positive x-axis. We use the same mesh as for Case 3. We estimate the value of the FOS to be about 1.16, which is 22% lower than in Case 3. The result seems to be reasonable for a value of $k_h = 0.1$ [91]. As expected, the serial and parallel SEMs (eight processors) are in perfect agreement. Because the pseudostatic seismic load extends failure more along the positive x-axis, the unstable volume is larger than in Case 3 (Figure 13b).

4.2. Example 1: Reservoir embankment

Having validated both the serial and parallel SEMs, let us consider the stability of an embankment. We construct a 3D model (Figure 14) from a 2D reservoir embankment model developed by Griffiths and Lane [45], which represents an actual reservoir with an earthen dam [123]. There are two main differences between this problem and the previous four cases. First, the model consists of two slopes with different angles; second, we need to include surface traction due to the reservoir (Figure 15). Therefore, we need to consider the effects of the gravity load, water pressure, and surface traction simultaneously. There is a constant traction on horizontal surfaces and a downwardly increasing traction on sloping submerged upstream surfaces (Figure 15). We again take advantage of the symmetry of the model and solve only for the symmetric half of the model with appropriate boundary conditions on the symmetry plane. The left and right faces are partially constrained along

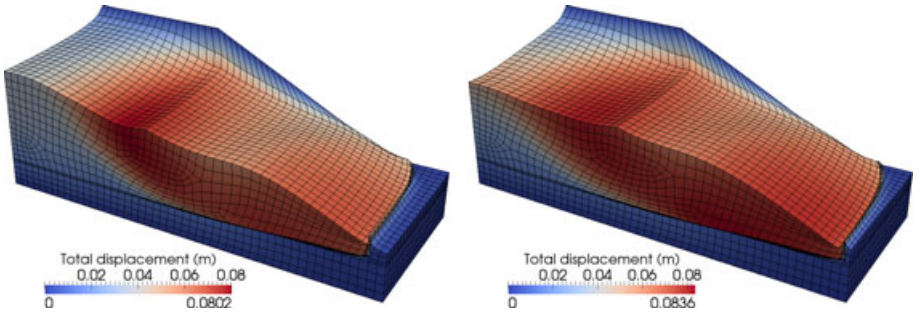

Figure 13. (a) Deformed volume at failure for Case 3. (b) Deformed volume at failure for Case 4. The results obtained by the serial and parallel spectral-finite methods were identical in both cases. Actual deformation is increased along the displacement vector for clearer visualization.

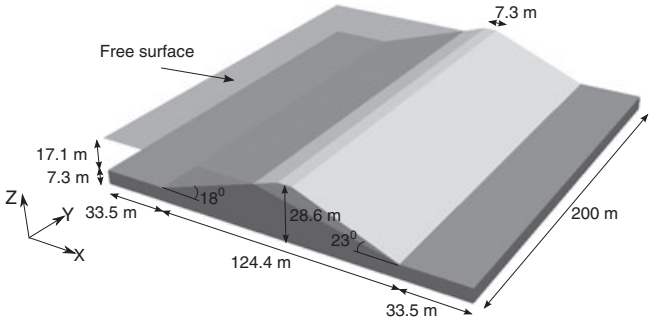

Figure 14. Reservoir embankment model: dry region (light gray) and wet region (dark gray). The top surfaces of the wet region mark the free surface. Dry and wet regions have the same material properties of unit weight $\gamma = 18.2$ kN/m^3, friction angle $\phi = 37^0$, and cohesion $c = 13.8$ kN/m^2. The dilation angle, Young's modulus, and Poisson's ratio are taken, respectively, as 0, 10^5 kN/m^2, and 0.3 for both regions.

DOI: 10.1002/nme

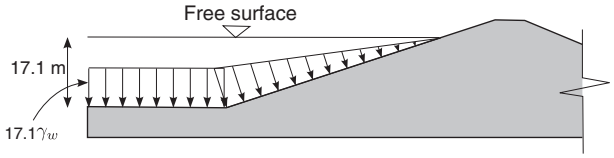

Figure 15. Cross section of the embankment showing surface traction on upstream surfaces due to the reservoir.

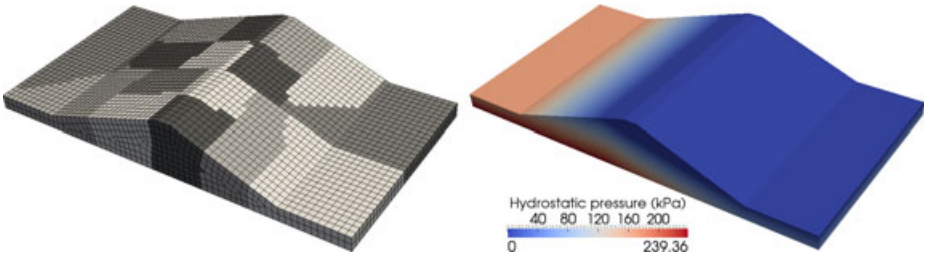

Figure 16. (a) Mesh of the symmetric half of the reservoir embankment model. The mesh is partitioned into 16 domains for parallel processing. (b) Hydrostatic pressure due to the reservoir.

the x-axis, the front and back faces are partially constrained along the y-axis, and the bottom face is fully constrained. Figure 16a shows the mesh for this model, which consists of 9669 elements with an average size of 3 m. The mesh is partitioned into 16 domains for parallel processing. Contrary to Case 3, we do not honor the water table during meshing. This avoids a possible reduction in mesh quality, in particular around sharp corners generated by the water table. With this meshing scheme, however, we need to test all the nodes to determine their submerged condition. The computed hydrostatic pressure is shown in Figure 16b.

We compute the FOS and potential failure surface for two possible scenarios: (1) the reservoir is filled, as shown in Figure 14; and (2) the reservoir is empty, corresponding to the drawdown stage or the stage before the reservoir was filled. Obviously, surface traction and hydrostatic pressure need not be considered in the second case. We use a relative tolerance of 10^{-8} for conjugate-gradient iterations and 5×10^{-4} for nonlinear iterations. From the maximum displacement curve (Figure 17), we estimate a FOS of about 2.54 for the empty reservoir and 1.91 for the filled reservoir. When the reservoir is filled, the FOS is reduced by about 25%, which is very important for safe design of the embankment. For the 2D model, Griffiths and Lane [45] estimated FOS values of 2.42 and 1.90 for the two cases using a limit equilibrium method, and FOS values of 2.5 and 1.9 using a FEM. Our results are in good agreement with these results. It may seem surprising that the 2D and 3D FOS values are almost identical, because the FOS for a 3D model is usually greater than that for the equivalent 2D model [40, 124]. However, because of boundary conditions and symmetry of the model, this problem is equivalent to a plain-strain problem. We should further note that the 3D FOS approaches the 2D FOS as the ratio of slope width to slope height increases [52, 55].

The downstream slope is steeper than the upstream slope. In case of a filled reservoir, the horizontal component of traction on the sloping face acts along the orientation of the downstream slope. As a result, it is more vulnerable than the upstream slope in both cases. Therefore, the downstream slope fails as shown in Figure 18a–b. In the case of a filled reservoir, however, the extent of failure is larger than for an empty reservoir, as expected.

4.3. Example 2: Large-scale mountain slope

Finally, we apply the method to a real slope at Åknes, which is an unstable mountain slope located in western Norway (Figure 19). Its unstable flank is moving at a mean rate of about 6 cm/year and as fast as 14 cm/year [125]. The sliding slope consists of mainly gneiss, densely jointed along the

DOI: 10.1002/nme

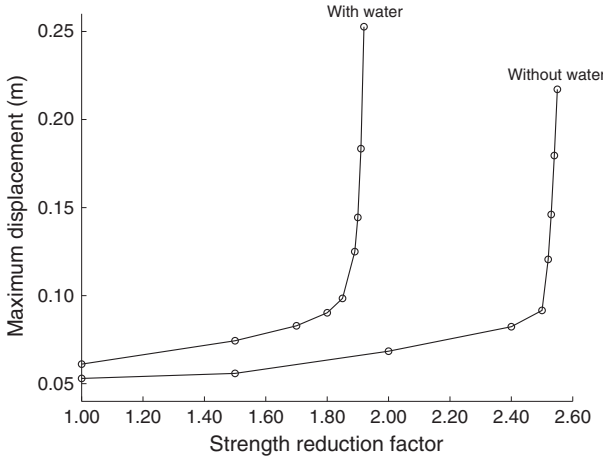

Figure 17. Maximum displacement at various strength reduction factors for two examples of an earthen embankment: with and without water.

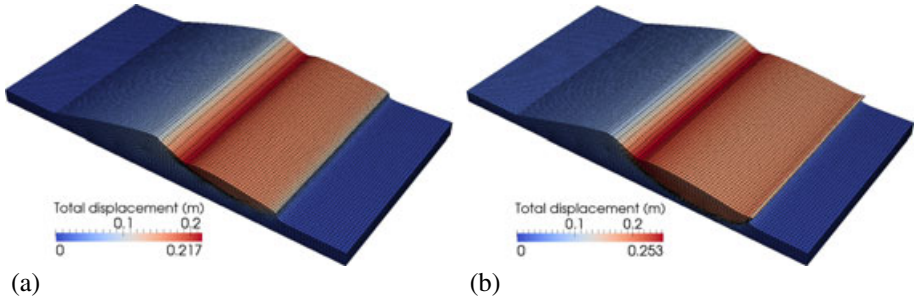

(a) (b)

Figure 18. Deformed volumes at failure for an earthen embankment: (a) without water and (b) with water. Actual deformation is increased along the displacement vector for clearer visualization.

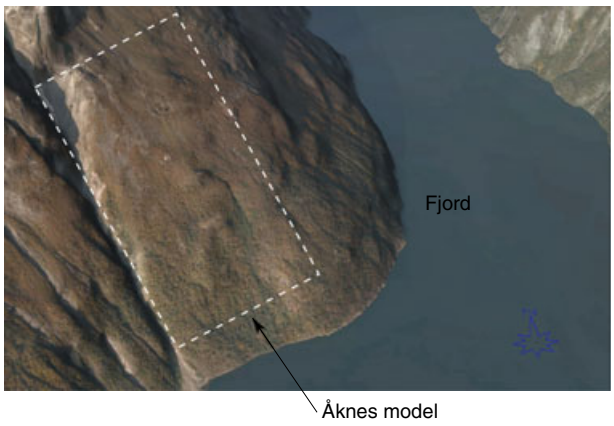

Figure 19. Åknes mountain slope in Norway. Source: `www.norgei3d.no`.

foliation, and its volume is approximately 35–40 million m^3 [125–127]. Because of its massive volume and proximity to the fjord, it poses a potential tsunami risk. Several monitoring instruments are in place for early warning, including a seismic network [128]. Although we do not have detailed information on the failure surface, it is important to know approximately how it will fail. Therefore, rather than determining a FOS, we compute elastoplastic deformation for a rather large FOS (we select 2.0) and determine its possible failure pattern. We use a digital elevation model map of the slope and build a 3D model as shown in Figure 20a. Kveldsvik *et al.* [126] have estimated the

DOI: 10.1002/nme

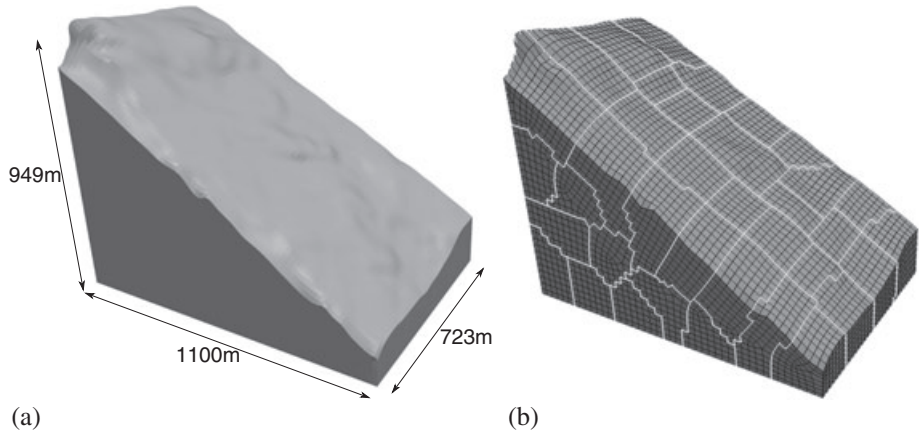

Figure 20. (a) Åknes mountain slope model. (b) Spectral-element mesh of the model. The mesh is partitioned into 64 domains for parallel computing. The white lines represent the computational domain interfaces, that is, the mesh slices for the parallel code.

material properties of the Åknes slope (Table II). Therefore, we use a homogeneous model based on these material properties. We take an approximate value of cohesion of 200 kN/m^2 for the densely jointed granitic rock.

The model is meshed with an average element size of 25 m, leading to a total number of 28,480 elements. The mesh is partitioned into 64 domains, as shown in Figure 20b. Because of the relatively coarse mesh, we use 4 GLL points in each direction, that is, 64 GLL points per element. We set a conjugate-gradient tolerance of 10^{-6} and a nonlinear tolerance of 5×10^{-4}. Because we do not have reliable information on the actual boundary conditions, we compute displacement fields with two different boundary conditions. In both cases, the front, back, and bottom surfaces are fully constrained, and the right surface is constrained only along the horizontal direction. In the first case, the left surface is fully constrained, whereas in the second case, the left surface is constrained only along the horizontal direction. The first case is more appropriate for the sound rock, whereas the second case is more appropriate for the weak rock.

Figure 21a–b show the displacement fields for the two cases. As expected, we observe slightly different displacement fields depending on the case. Consequently, the collapse patterns are also slightly different (Figure 22a–b). In case of a partially constrained left face, larger displacements are observed along the left surface. The collapse patterns are more or less circular because we have taken a homogeneous model. Because the boundary conditions influence the stability of the slope, it is important to apply appropriate boundary conditions [129]. For this particular problem, an even bigger model domain may be required to mimic a semi-infinite medium, so that the domain boundaries are sufficiently far from the failure surface.

4.4. Parallel performance

Using the Åknes model, we conduct a strong-scaling performance test, that is, we measure the computation time for various numbers of processors while keeping the problem size fixed. We run the program on 16, 32, 48, 64, and 80 processors. The results shown in Figure 23 demonstrate that

Table II. Material properties for the Åknes slope model.

Unit weight	26.86 kN/m^3
Young's modulus	40^9 kN/m^3
Poisson's ratio	0.13
Cohesion	200 kN/m^2
Friction angle	27.6^0
Dilation angle	13.8^0

DOI: 10.1002/nme

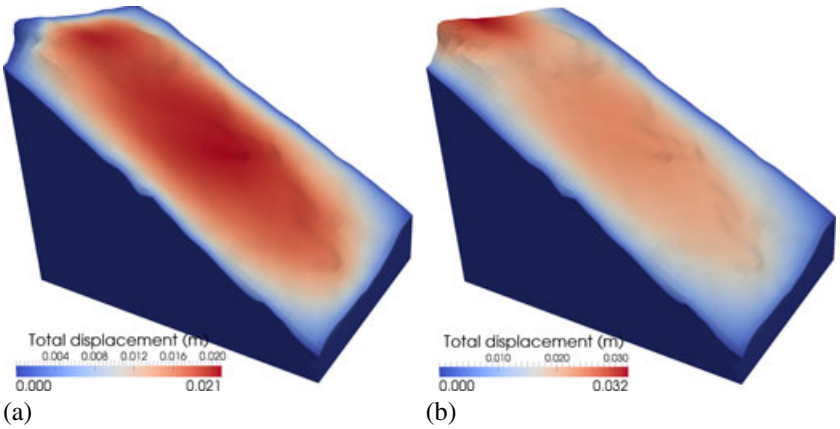

Figure 21. Total displacement at a strength reduction factor of 2.0. (a) Left face fully constrained. (b) Left face partially constrained.

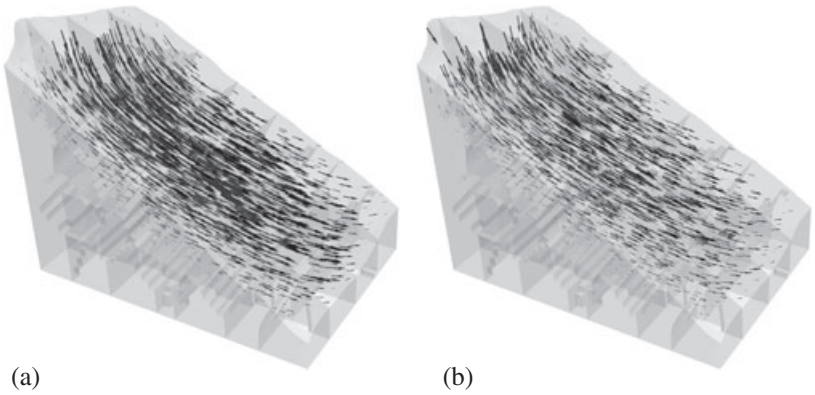

Figure 22. Displacement vectors at a strength reduction factor of 2.0. (a) Left face fully constrained. (b) Left face partially constrained. Vector fields in each figure are independently scaled to their range. The shaded surfaces represent the interfaces of the partitioned domains used for parallel computing.

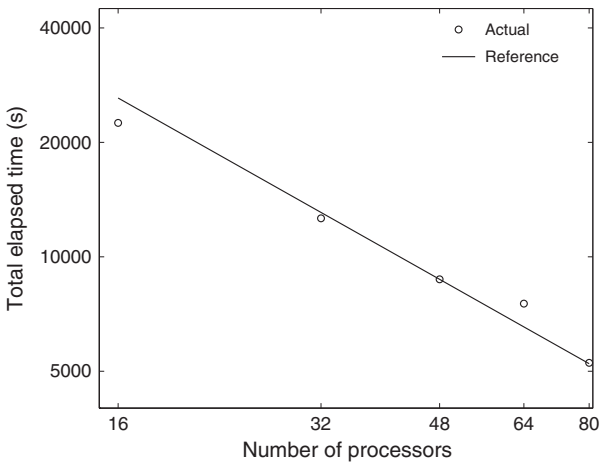

Figure 23. Total elapsed time for a fixed problem size run on 16, 32, 48, 64, and 80 processors, compared with a reference line computed using the total elapsed time for 48 processors, and assuming perfect linear scaling.

DOI: 10.1002/nme

the code performs reasonably well for large-scale problems. In the future, it may be important to implement reverse Cuthill–McKee sorting of the degrees of freedom and bandwidth reduction of the element adjacency matrix [130], renumbering nodes to enhance parallel performance [131]. In the future, graphics processing unit could be utilized to further improve the performance [132–134].

5. DISCUSSION AND CONCLUSIONS

We have implemented a SEM for 3D elastoplastic problems in geomechanics and developed a versatile open-source software package for slope stability analysis. The numerical method is parallelized on the basis of domain decomposition. We successfully compared the results of our simulations with a classical FEM as well as limit equilibrium methods. We currently need to input possible SRFs manually. In the future, it would be useful to implement an automatic procedure to find the possible FOS using simple root finding methods, such as the bisection method [117]. Results obtained for an earthen embankment are in excellent agreement with 2D results from the literature. Simulation of a mountain slope at Åknes illustrates potential applications of the software to complex and large-scale slopes. Considering the fact that the rock mass at Åknes is heavily jointed, it would be of future interest to use the Hoek–Brown failure criterion [135]. We plan to include more realistic model parameters and boundary conditions to perform more relevant simulations. With such detailed models, it would be possible to predict long-term creep behavior of the Åknes rock slope. In our examples, we have used an almost uniform mesh size. In the future, it would be helpful to use a geometrically adaptive mesh for large-scale problems.

For other elastoplastic problems, using a more accurate and efficient integration algorithm for the elastoplastic constitutive relation may be important, for example, a modified Euler method, in particular one with automatic error control on load stepping [136, 137] and a return mapping with a tangent stiffness approach [32, 138].

We envisage further developments for geodynamic problems related to glacial rebound and postseismic relaxation with the inclusion of viscoelasticity, for example, based on a generalized Maxwell rheology. Finally, thus far we have implemented only material nonlinearity. Geometrical nonlinearity could be implemented for the analysis of large displacements, for example, based on adaptive mesh refinement.

Our software is open source, and the entire package SPECFEM3D_GEOTECH is freely available via `www.geodynamics.org`.

ACKNOWLEDGEMENTS

We thank Michael Roth, Valérie Maupin, and Daniela Kühn for their helpful discussions and suggestions. We thank Åknes/Tafjord Beredskap IKS (`www.aknes.no`) for the Åknes digital elevation map. Parallel programs were run on the Titan cluster owned by the University of Oslo and the Norwegian metacenter for High Performance Computing (NOTUR), and at the Princeton Institute for Computational Science and Engineering (PICSciE), USA. 3D data were visualized using the open-source parallel visualization software ParaView/VTK (`www.paraview.org`). This work was funded in part by the Research Council of Norway and supported by industry partners BP, Statoil, and Total. We thank two anonymous reviewers for their insightful comments.

REFERENCES

1. Hughes TJR. *The Finite Element Method: Linear Static and Dynamic Finite Element Analysis*. Prentice-Hall: Englewood Cliffs, NJ, 1987.
2. Bathe KJ. *Finite Element Procedures*. Prentice Hall: Englewood Cliffs, NJ, 1995.
3. Zienkiewicz OC, Taylor RL. *The Finite Element Method for Solid and Structural Mechanics*. Elsevier Butterworth-Heinemann: Burlington, MA, 2005.
4. Price MA, Armstrong CG. Hexahedral mesh generation by medial surface subdivision: Part II. Solids with flat and concave edges. *International Journal for Numerical Methods in Engineering* 1997; **40**(1):111–136.
5. Tautges TJ. The generation of hexahedral meshes for assembly geometry: survey and progress. *International Journal for Numerical Methods in Engineering* 2001; **50**(12):2617–2642.
6. Shepherd J, Johnson C. Hexahedral mesh generation constraints. *Engineering with Computers* 2008; **24**:195–213.

DOI: 10.1002/nme

7. Sandia National Laboratories. Cubit 13.0 User Documentation, 2011. Available from: cubit.sandia.gov,[Online; accessed 27-May-2011].
8. Rainsberger R. *TrueGrid User's Manual*, version 2.3.0. XYZ Scientific Applications, Inc.: Livermore, CA, 2006. Available from: www.truegrid.com.
9. Geuzaine C, Remacle JF. GMSH: a three-dimensional finite element mesh generator with built-in pre- and post-processing facilities. *International Journal for Numerical Methods in Engineering* 2009; **79**(11):1309–1331.
10. Hesthaven JS, Teng CH. Stable spectral methods on tetrahedral elements. *SIAM Journal on Scientific Computing* 1999; **21**(6):2352–2380.
11. Taylor MA, Wingate BA. A generalized diagonal mass matrix spectral element method for non-quadrilateral elements. *Applied Numerical Mathematics* 2000; **33**(1–4):259–265.
12. Komatitsch D, Martin R, Tromp J, Taylor MA, Wingate BA. Wave propagation in 2-D elastic media using a spectral element method with triangles and quadrangles. *Journal of Computational Acoustics* 2001; **9**:703–718.
13. Mercerat ED, Vilotte JP, Sánchez-Sesma FJ. Triangular spectral element simulation of two-dimensional elastic wave propagation using unstructured triangular grids. *Geophysical Journal International* 2006; **166**:679–698.
14. Davis P, Rabinowitz P. *Methods of Numerical Integration*. Dover Publications: Mineola, NY, 2007.
15. Durufle M, Grob P, Joly P. Influence of Gauss and Gauss–Lobatto quadrature rules on the accuracy of a quadrilateral finite element method in the time domain. *Numerical Methods for Partial Differential Equations* 2009; **25**:526–551.
16. Seriani G, Oliveira SP. Dispersion analysis of spectral-element methods for elastic wave propagation. *Wave Motion* 2008; **45**:729–744. DOI: 10.1016/j.wavemoti.2007.11.007.
17. De Basabe JD, Sen MK. Stability of the high-order finite elements for acoustic or elastic wave propagation with high-order time stepping. *Geophysical Journal International* 2010; **181**(1):577–590.
18. Patera AT. A spectral element method for fluid dynamics: laminar flow in a channel expansion. *Journal of Computational Physics* 1984; **54**:468–488.
19. Canuto C, Hussaini MY, Quarteroni A, Zang TA. *Spectral Methods in Fluid Dynamics*. Springer: New York, 1988.
20. Cohen G. *Higher-order Numerical Methods for Transient Wave Equations*. Springer-Verlag: Berlin, Germany, 2002.
21. Deville MO, Fischer PF, Mund EH. *High-order Methods for Incompressible Fluid Flow*. Cambridge University Press: Cambridge, United Kingdom, 2002.
22. Seriani G. 3-D large-scale wave propagation modeling by spectral element method on Cray T3E multiprocessor. *Computer Methods in Applied Mechanics and Engineering* 1994; **164**:235–247.
23. Faccioli E, Maggio F, Paolucci R, Quarteroni A. 2D and 3D elastic wave propagation by a pseudo-spectral domain decomposition method. *Journal of Seismology* 1997; **1**(3):237–251.
24. Komatitsch D, Vilotte JP. The spectral element method: an efficient tool to simulate the seismic response of 2D and 3D geological structures. *Bulletin of the Seismological Society of America* 1998; **88**(2):368–392.
25. Komatitsch D, Tromp J. Introduction to the spectral element method for three-dimensional seismic wave propagation. *Geophysical Journal International* 1999; **139**:806–822.
26. Komatitsch D, Tromp J. Spectral-element simulations of global seismic wave propagation – I. Validation. *Geophysical Journal International* 2002; **149**:390–412.
27. Tromp J, Komatitsch D, Liu Q. Spectral-element and adjoint methods in seismology. *Communications in Computational Physics* 2008; **3**(1):1–32.
28. Oye V, Gharti HN, Aker E, Kühn D. Moment tensor analysis and comparison of acoustic emission data with synthetic data from spectral element method. *SEG Technical Program Expanded Abstracts* 2010; **29**(1):2105–2109. DOI: 10.1190/1.3513260.
29. Peter D, Komatitsch D, Luo Y, Martin R, Le Goff N, Casarotti E, Le Loher P, Magnoni F, Liu Q, Blitz C, Nissen-Meyer, T, Basini P, Tromp J. Forward and adjoint simulations of seismic wave propagation on fully unstructured hexahedral meshes. *Geophysical Journal International* 2011; **186**(2):721–739.
30. di Prisco C, Stupazzini M, Zambelli C. Nonlinear SEM numerical analyses of dry dense sand specimens under rapid and dynamic loading. *International Journal for Numerical and Analytical Methods in Geomechanics* 2007; **31**:757–788.
31. Babuska I, Suri M. The *p*- and *h-p* versions of the finite element method, an overview. *Computer Methods in Applied Mechanics and Engineering* 1990; **80**:5–26.
32. Simo JC, Hughes TJR. *Computational Inelasticity*. Springer: New York, 1998.
33. Schwab C. *p- and hp- Finite Element Methods: Theory and Applications to Solid and Fluid Mechanics*. Oxford University Press: USA, 1999.
34. Belytschko T, Liu WK, Moran B. *Nonlinear Finite Elements for Continua and Structures*. Wiley: West Sussex, England, 2000.
35. Luccioni LX, Pestana JM, Taylor RL. Finite element implementation of non-linear elastoplastic constitutive laws using local and global explicit algorithms with automatic error control. *International Journal for Numerical Methods in Engineering* 2001; **50**:1191–1212.
36. Dupros F, De Martin F, Foerster E, Komatitsch D, Roman J. High-performance finite-element simulations of seismic wave propagation in three-dimensional nonlinear inelastic geological media. *Parallel Computing* 2010; **36**:308–325.
37. Abramson LW, Lee TS, Sharma S, Boyce GM. *Slope Stability and Stabilization Methods*. Wiley: New York, 1995.
38. Cheng YM, Lau CK. *Slope Stability Analysis and Stabilization: New Methods and Insight*. Routledge: New York, 2008.

DOI: 10.1002/nme

39. Duncan JM, Wright SG. *Soil Strength and Slope Stability*. John Wiley & Sons: Hoboken, NJ, 2005.
40. Hungr O. An extension of Bishop's simplified method of slope stability analysis to three dimensions. *Géotechnique* 1987; **37**:113–117.
41. Xing Z. Three-dimensional stability analysis of concave slopes in plan view. *Journal of Geotechnical Engineering* 1988; **114**(6):658–671.
42. Lam L, Fredlund DG. A general limit equilibrium model for three-dimensional slope stability analysis. *Canadian Geotechnical Journal* 1993; **30**:905–919.
43. Zhu D, Lee CF, Jiang HD. Generalized framework of limit equilibrium methods for slope stability analysis. *Géotechnique* 2003; **53**(4):377–395.
44. Razdolsky AG. Slope stability analysis based on the direct comparison of driving forces and resisting forces. *International Journal for Numerical and Analytical Methods in Geomechanics* 2009; **33**(8):1123–1134.
45. Griffiths DV, Lane PA. Slope stability analysis by finite elements. *Géotechnique* 1999; **49**:387–403.
46. Drücker DC, Prager W, Greenberg HJ. Extended limit design theorems for continuous media. *Quarterly of Applied Mathematics* 1952; **9**(4):381–389.
47. Chen WF. *Limit Analysis and Soil Plasticity*. Elsevier Science: Amsterdam, The Netherlands, 1975.
48. Salençon J. An introduction to the yield design theory and its application to soil mechanics. *European Journal of Mechanics A/Solids* 1990; **9**(5):477–500.
49. Sloan SW. Lower bound limit analysis using finite elements and linear programming. *International Journal for Numerical and Analytical Methods in Geomechanics* 1988; **12**:61–77.
50. Lyamin AV, Sloan SW. Lower bound limit analysis using non-linear programming. *International Journal for Numerical Methods in Engineering* 2002; **55**:573–611.
51. Chen Z, Wang X, Haberfield C, Yin J, Wang Y. A three-dimensional slope stability analysis method using the upper bound theorem. Part I: theory and methods. *International Journal of Rock Mechanics and Mining Sciences* 2001; **38**(3):369–378.
52. Michalowski RL. Limit analysis and stability charts for 3D slope failures. *Journal of Geotechnical and Geoenvironmental Engineering* 2010; **136**(4):583–593.
53. Yu HS, Salgado R, Sloan SW, Kim JM. Limit analysis versus limit equilibrium for slope stability. *Journal of Geotechnical and Geoenvironmental Engineering* 1998; **124**(1):1–11.
54. Lyamin AV, Sloan SW. Upper bound limit analysis using linear finite elements and non-linear programming. *International Journal for Numerical and Analytical Methods in Geomechanics* 2002; **26**(2):181–216.
55. Griffiths DV, Marquez RM. Three-dimensional slope stability analysis by elasto-plastic finite elements. *Géotechnique* 2007; **57**:537–546.
56. Smith GD. *Numerical Solution of Partial Differential Equations: Finite Difference Methods*, 3rd edn. Oxford University Press: USA, 1985.
57. Reddy JN. *Introduction to the Finite Element Method*. McGraw-Hill: New York, NY, 1993.
58. Smith IM, Hobbs R. Finite element analysis of centrifuged and built-up slopes. *Géotechnique* 1974; **24**:531–559.
59. Zienkiewicz OC, Humpheson C, Lewis RW. Associated and non-associated viscoplasticity and plasticity in soil mechanics. *Géotechnique* 1975; **25**:671–689.
60. Griffiths DV. Finite element analysis of walls, footings and slopes. In *Proceedings of the symposium on computer applications to geotechnical problems in highway engineering*, Randolph MF (ed.). PM Geotechnical Analysts Ltd: Cambridge, UK, 1980; 122–146.
61. Sainak AN. Application of three-dimensional finite element method in parametric and geometric studies of slope stability. *Advances in geotechnical engineering (Skempton conference)* 2004; **2**:933–942.
62. Li X. Finite element analysis of slope stability using a nonlinear failure criterion. *Computers and Geotechnics* 2007; **34**(3):127–136.
63. Fredlund DG, Scoular REG. Using limit equilibrium concepts in finite element slope stability analysis. *Proceedings of the International Symposium on Slope Stability Engineering-IS-Shikoku'99*, Matsuyama, Shikoku, Japan, 1999; 31–47.
64. Chen J, Yin JH, Lee CF. Upper bound limit analysis of slope stability using rigid finite elements and nonlinear programming. *Canadian Geotechnical Journal* 2003; **40**:742–752.
65. Kinakin D, Stead D. Analysis of the distributions of stress in natural ridge forms: implications for the deformation mechanisms of rock slopes and the formation of sackung. *Geomorphology* 2005; **65**:85–100.
66. Bozzano F, Lenti L, Martino S, Montagna A, Paciello A. Earthquake triggering of landslides in highly jointed rock masses: reconstruction of the 1783 Scilla rock avalanche (Italy). *Geomorphology* 2011; **129**(3–4):294–308.
67. Jing L, Stephansson O. *Fundamentals of Discrete Element Methods for Rock Engineering: Theory and Applications*. Elsevier Science: Amsterdam, The Netherlands, 2007.
68. Cundall PA. A computer model for simulating progressive large scale movements in blocky rock systems. *ISRM Symp., Proc. 2*, Nancy, France, 1971; 129–136.
69. Cundall PA, Strack ODL. A discrete numerical model for granular assemblies. *Géotechnique* 1979; **29**(1):47–65.
70. Chuhan Z, Pekau OA, Feng J, Guanglun W. Application of distinct element method in dynamic analysis of high rock slopes and blocky structures. *Soil Dynamics and Earthquake Engineering* 1997; **16**(6):385–394.
71. Itasca. Itasca software products – FLAC, FLAC3D, PFC2D, PFC3D, UDEC, and 3DEC, 2004. Available from: www.itascacg.com.
72. Calvetti F, Crosta G, Tatarella M. Numerical simulation of dry granular flows: from the reproduction of small-scale expriments to the prediction of rock avalanches. *Rivista Italiana Geotecnica* 2000; **XXXIV**(2):21–38.

DOI: 10.1002/nme

73. Havenith HB, Strom A, Calvetti F, Jongmans D. Seismic triggering of lanslides. Part B: simulation of dynamic failure processes. *Natural Hazards and Earth System Sciences* 2003; **3**:663–682.
74. Eberhardt E, Stead D, Coggan J. Numerical analysis of initiation and progressive failure in natural rock slopes – the 1991 Randa rockslide. *International Journal of Rock Mechanics and Mining Sciences* 2004; **41**(1):69–87.
75. Kuo CY, Tai YC, Bouchut F, Mangeney A, Pelanti M, Chen RF, Chang KJ. Simulation of Tsaoling landslide, Taiwan, based on Saint Venant equations over general topography. *Engineering Geology* 2009; **104**(1–4):181–189.
76. Tang CL, Hu JC, Lin ML, Angelier J, Lu CY, Chan YC, Chu HT. The Tsaoling landslide triggered by the Chi-Chi earthquake, Taiwan: insights from a discrete element simulation. *Engineering Geology* 2009; **106**:1–19.
77. Campbell CS, Cleary PW, Hopkins M. Large-scale landslide simulations: global deformation velocities and basal friction. *Journal of Geophysical Research* 1995; **100**:8267–8283.
78. Valdivia C, Lorig L. Slope stability at Escondida mine. In *Slope stability in surface mining*, Hustrulid WA, McCarter MK, Van Zyl DJA (eds). Society for Mining Metallurgy & Exploration: Littleton, CO, 2000; 153–162.
79. Munjiza A. *The Combined Finite-discrete Element Method*. John Wiley and Sons: West Sussex, England, 2004.
80. Rockfield Software Ltd. ELFEN 2D/3D numerical modelling package, 2004. Available from: www.rockfield.co.uk.
81. Stead D, Eberhardt E, Coggan JS. Developments in the characterization of complex rock slope deformation and failure using numerical modelling techniques. *Engineering Geology* 2006; **83**:217–235.
82. Monaghan JJ. Smoothed particle hydrodynamics. *Annual Review of Astronomy and Astrophysics* 1992; **30**:543–574.
83. Bui HH, Fukagawa R, Sako K, Wells JC. Slope stability analysis and discontinuous slope failure simulation by elasto-plastic smoothed particle hydrodynamics (SPH). *Géotechnique* 2011; **61**(7):565–574.
84. Belytschko T, Black T. Elastic crack growth in finite elements with minimal remeshing. *International Journal for Numerical Methods in Engineering* 1999; **45**(5):601–620.
85. Sukumar N, Moës N, Moran B, Belytschko T. Extended finite element method for three-dimensional crack modeling. *International Journal for Numerical Methods in Engineering* 2000; **48**(11):1549–1570.
86. Hori M, Oguni K, Sakaguchi H. Proposal of FEM implemented with particle discretization for analysis of failure phenomena. *Journal of the Mechanics and Physics of Solids* 2005; **53**(3):681–703.
87. Oguni K, Wijerathne MLL, Okinaka T, Hori M. Crack propagation analysis using PDS-FEM and comparison with fracture experiment. *Mechanics of Materials* 2009; **41**(11):1242–1252.
88. Sanborn SE, Prévost JH. Frictional slip plane growth by localization detection and the extended finite element method (XFEM). *International Journal of Numerical and Analytical Methods in Geomechanics* 2011; **35**(11):1278–1298.
89. Hughes TJR, Levit I, Winget J. An element-by-element solution algorithm for problems of structural and solid mechanics. *Computer Methods in Applied Mechanics and Engineering* 1983; **36**(2):241–254.
90. Lorig L, Varona P. Practical slope-stability analysis using finite-difference codes. In *Slope stability in surface mining*, Hustrulid WA, McCarter MK, Van Zyl DJA (eds). Society for Mining Metallurgy & Exploration: Littleton, CO, 2000; 153–162.
91. Kramer SL. *Geotechnical Earthquake Engineering*. Prentice Hall: Upper Saddle River, NJ, 1996.
92. Li AJ, Lyamin AV, Merifield RS. Seismic rock slope stability charts based on limit analysis methods. *Computers and Geotechnics* 2009; **36**(1–2):135–148.
93. Terzaghi K. *Engineering geology (Berkey) Volume, chap.* Mechanisms of Landslides. Geological Society of America: New York, NY, 1950.
94. Seed HB. Considerations in the earthquake-resistant design of earth and rockfill dams. *Géotechnique* 1979; **29**:215–263.
95. Hynes-Griffin ME, Franklin AG. Rationalizing the seismic coefficient method. *Technical Report*, US Army Corps of Engineers waterways experiment station, 1984.
96. Seed HB, Makdisi FI, Idriss IM, Lee KL. The slides in the San Fernando dams during the earthquake of February 9, 1971. *Journal of the Geotechnical Engineering Division* 1975; **101**:651–688.
97. Marcuson WF, Ballard RF, Ledbetter RH. Liquefaction failure of tailings dams resulting from the Near Izu Oshima earthquake, 14 and 15 January, 1978. *6th Pan American Conference on Soil Mechanics and Foundation Engineering*, Lima, Peru, 1979.
98. Schofield AN, Wroth CP. *Critical State Soil Mechanics*. McGraw-Hill: New York, NY, 1968.
99. Coussy O. *Poromechanics*, (2nd edn). Wiley: West Sussex, England, 2004.
100. Zienkiewicz O, Cormeau I. Visco-plasticity–plasticity and creep in elastic solids – a unified numerical solution approach. *International Journal for Numerical Methods in Engineering* 1974; **8**(4):821–845.
101. Smith IM, Griffiths DV. *Programming the Finite Element Method*. John Wiley & Sons: West Sussex, England, 2004.
102. Thomas JN. An improved accelerated initial stress procedure for elasto-plastic finite element analysis. *International Journal for Numerical and Analytical Methods in Geomechanics* 1984; **8**:359–379.
103. Gropp W, Lusk E, Skjellum A. *Using MPI, Portable Parallel Programming with the Message-passing Interface*. MIT Press: Cambridge, USA, 1994.
104. Pacheco P. *Parallel Programming with MPI*. Morgan Kaufmann: San Francisco, CA, 1997.
105. Pellegrini F, Roman J. SCOTCH: a software package for static mapping by dual recursive bipartitioning of process and architecture graphs. *Lecture Notes in Computer Science* 1996; **1067**:493–498.
106. Chevalier C, Pellegrini F. PT-SCOTCH: a tool for efficient parallel graph ordering. *Parallel Computing* 2008; **34**(6–8):318–331.

DOI: 10.1002/nme

107. Karypis G, Kumar V. Multilevel k-way partitioning scheme for irregular graphs. *Journal of Parallel and Distributed Computing* 1998; **48**(1):96–129.
108. Sobh NA, Gustafson K. Preconditioned conjugate gradient and finite element methods for massively data-parallel architectures. *Computer Physics Communications* 1991; **65**:253–267.
109. Khan AI, Topping BHV. Parallel finite element analysis using Jacobi-conditioned conjugate gradient algorithm. *Advances in Engineering Software* 1996; **25**:309–319.
110. Liu Y, Zhou W, Yang Q. A distributed memory parallel element-by-element scheme based on Jacobi-conditioned conjugate gradient for 3D finite element analysis. *Finite Elements in Analysis and Design* 2007; **43**: 494–503.
111. Nakajima K, Okuda H. Parallel iterative solvers with localized ILU preconditioning for unstructured grids on workstation clusters. *International Journal of Computational Fluid Dynamics* 1999; **12**(3):315–322.
112. Matsui T, San KC. Finite element slope stability analysis by strength reduction technique. *Soils and foundations* 1992; **32**:59–70.
113. Manzari MT, Nour MA. Significance of soil dilatancy in slope stability analysis. *Journal of Geotechnical and Geoenvironmental Engineering* 2000; **126**(1):75–80.
114. Snitbhan N, Chen WF. Elastic-plastic large deformation analysis of soil slopes. *Computers & structures* 1976; **9**:567–577.
115. Dunlop P, Duncan JM. Development of failure around excavated slopes. *Journal of the Soil Mechanics and Foundations Division* 1970; **96**:471–493.
116. Chen JX, Ke PZ, Zhang G. Slope stability analysis by strength reduction elasto-plastic FEM. *Key Engineering Materials* 2007; **345-346**:625–628.
117. Dawson EM, Roth WH, Drescher A. Slope stability analysis by strength reduction. *Géotechnique* 1999; **49**:835–840.
118. Zheng H, Liu DF, Li CG. Slope stability analysis based on elasto-plastic finite element method. *International Journal for Numerical Methods in Engineering* 2005; **64**:1871–1888.
119. Duan QW, Wang YJ, Zhang PW. Study on deformation parameter reduction technique for the strength reduction finite element method. In *Landslides and Engineered Slopes: From the Past to the Future*, Chen ZY, Zhang JM, Ho K (eds). Taylor & Francis: London, UK, 2008; 663–669.
120. Hammah R, Yacoub T, Corkum B, Curran J. A comparison of finite element slope stability analysis with conventional limit-equilibrium investigation. *Proceedings of the 58th Canadian Geotechnical and 6th Joint IAH-CNC and CGS Groundwater Specialty Conferences – GeoSask 2005*, Saskatoon, Canada, 2005.
121. Fredlund DG, Krah J. Comparison of slope stability methods of analysis. *Canadian Geotechnical Journal* 1977; **14**:429–439.
122. Hungr O. *Clara 2.31: Slope Stability in Two or Three Dimensions for IBM Compatible Microcomputers*. O. Hungr Geotechnical Research Inc.: Vancouver, 1988.
123. Paice GM. Finite element analysis of stochastic soils. *PhD Thesis*, University of Manchester, U.K., 1997.
124. Hutchinson JN, Sarma SK. Discussion on 'Three-dimensional limit equilibrium analysis of slope'. *Géotechnique* 1985; **35**:215.
125. Ganerød GV, Grøneng G, Rønning JS, Dalsegg E, Elvebakk H, Tønnesen JF, Kveldsvik V, Eiken T, Blikra LH, Braathen A. Geological model of the Åknes rockslide, western Norway. *Engineering Geology* 2008; **102**(1-2): 1–18.
126. Kveldsvik V, Nilsen B, Einstein HH, Nadim F. Alternative approaches for analyses of a 100,000 m^3 rock slide based on Barton–Bandis shear strength criterion. *Landslides* 2008; **5**(2):161–176.
127. Kveldsvik V, Einstein HH, Nilsen B, Blikra LH. Numerical analysis of the 650,000 m^2 Åknes rock slope based on measured displacements and geotechnical data. *Rock Mechanics and Rock Engineering* 2009; **42**:689–728.
128. Roth M, Blikra LH. Seismic monitoring of the unstable rock slope at Åknes, Norway. *EGU general assembly 2009, Vienna, Austria, abstract #EGU2009-3680* 2009; **11**:3680.
129. Chung AK. On the boundary conditions in slope stability analysis. *International Journal for Numerical and Analytical Methods in Geomechanics* 2003; **27**:905–926.
130. Cuthill E, McKee J. Reducing the bandwidth of sparse symmetric matrices. In *Proceedings of the 24th National ACM Conference*. ACM Press: New York, 1969; 157–172.
131. Komatitsch D, Labarta J, Michéa D. A simulation of seismic wave propagation at high resolution in the inner core of the Earth on 2166 processors of MareNostrum. In *High Performance Computing for Computational Science – VECPAR 2008*, Palma JM, Amestoy PR, Daydé M, Mattoso M, Lopes JaC (eds). Springer-Verlag: Berlin, Heidelberg, 2008; 364–377.
132. Göddeke D, Strzodka R, Mohd-Yusof J, McCormick P, Buijssen SHM, Grajewski M, Turek S. Exploring weak scalability for FEM calculations on a GPU-enhanced cluster. *Parallel Computing* 2007; **33**(10-11):685–699.
133. Komatitsch D, Michéa D, Erlebacher G. Porting a high-order finite-element earthquake modeling application to NVIDIA graphics cards using CUDA. *Journal of Parallel and Distributed Computing* 2009; **69**(5): 451–460.
134. Komatitsch D, Erlebacher G, Göddeke D, Michéa D. High-order finite-element seismic wave propagation modeling with MPI on a large GPU cluster. *Journal of Computational Physics* 2010; **229**(20):7692–7714.
135. Hoek E, Carranza-Torres C, Corkum B. Hoek–Brown failure criterion – 2002 edition. *Proceedings of the Fifth North American Rock Mechanics Symposium, vol. 1*, University of Toronto Press: Toronto, Ontario, 2002; 267–273.

DOI: 10.1002/nme

136. Abbo AJ, Sloan SW. An automatic load stepping algorithm with error control. *International Journal for Numerical Methods in Engineering* 1996; **39**:1737–1759.
137. Sloan SW, Abbo AJ, Sheng D. Refined explicit integration of elastoplastic models with automatic error control. *Engineering Computations* 2001; **18**:121–194.
138. de Souza Neto EA, Perić D, Owen DRJ. *Computational Methods for Plasticity: Theory and Applications*. Wiley: West Sussex, England, 2009.

DOI: 10.1002/nme